

Contents

1	Introduction	1
2	Theory	1
2.1	Radioactive Decay	1
2.2	Decay schemes	3
2.3	Interaction of Electromagnetic Radiation with Matter	4
3	Electronic Devices	4
4	Setup and Execution of the Experiment	8
4.1	Part 1: Evaluation of the Thorium Spectrum	8
4.2	Part 2: Angle Dependency of Pair Annihilation	11
5	Data Analysis: Evaluation of the Thorium Spectrum	18
5.1	Energy calibration	18
5.2	Examination of the ^{228}Th spectrum	22
5.3	Examination of the underground spectrum	22
5.4	Interpretation of the ^{228}Th spectrum	24
5.5	Interpretation of the underground spectrum	25
6	Data Analysis: Angle Dependency of Pair Annihilation	26
6.1	Coincidence measurement	26
7	Summary and Discussion	28
7.1	Thorium Spectrum	28
7.2	Coincidence Measurement	29
A	Appendix	30
	List of Figures	30
	List of Tables	30
	Bibliography	31
A.1	Thorium Spectrum with Logarithmic y-scale	32
A.2	Close up peaks	33
A.3	Lab Notes	41

1 Introduction

In this experiment, we will analyze decay spectra of various isotopes and study the angle dependency of pair annihilation. Another purpose of this experiment is to gain a deeper understanding in scintillators, analog electronics and the NIM standards.

In the first part of this experiment, we will analyze the spectrum of thorium with an inorganic NaI scintillator. At first, the spectra of sodium (^{22}Na), cobalt (^{60}Co) and europium (^{152}Eu) are recorded and used for an energy calibration. Then the energy calibration is used to evaluate the thorium spectrum.

In the second part of the experiment, the NaI scintillator is used together with an organic plastic scintillator to examine the angle dependency of photons emitted by pair annihilation.

2 Theory

In this section we will talk about different types of radioactive decay as well as the effects relevant for this experiment. We will also explain interaction of electromagnetic radiation with matter and talk about the electronic devices used to carry out the experiment and process the signals.

If not specified otherwise, the information in this chapter is taken from the manual [1].

2.1 Radioactive Decay

Radioactive decay happens when an instable nucleus loses energy by emitting radiation. The rate of change of the number of nuclei is described by

$$\frac{dN}{dt} = -\lambda N, \quad (1)$$

where N is the number of nuclei and λ is a constant of decay specific to the material described.

Integrating eq. (1) leads to

$$N(t) = N_0 \exp(-\lambda t) \quad (2)$$

for the number N of nuclei with respect to time. N_0 represents the number of nuclei at a time $t = 0$.

Using eq. (2) it is easy to calculate the half-time

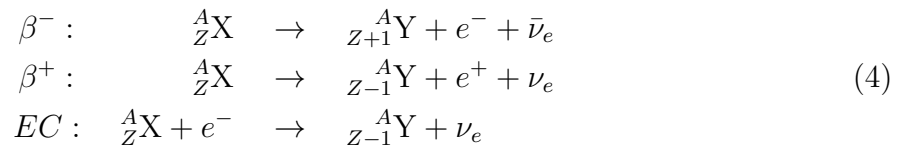
$$T_{1/2} = \frac{\log 2}{\lambda}, \quad (3)$$

after which half the original number of nuclei have decayed.

Types of radioactive decay include α -decay, β -decay and γ -decays.

α -decay An atomic nucleus ${}^A_Z\text{X}$ emits a so called α -particle and decays into a different nucleus ${}^{A-4}_{Z-2}\text{Y}$. The emitted α -particle is a ${}^4_2\text{He}$ -nucleus. Because the α -particle has a kinetic energy, the original nucleus must at least have a mass of the sum of the α -particle and the resulting nucleus, for the decay to occur.

β -decay There are three different types of β -decay, which are called β^- -decay, β^+ -decay and electron capture (EC):



For β^- -decay, a neutron from the nucleus is converted into a proton. Due to this process, an electron and a anti electron neutrino are emitted. This often happens in isotopes with neutron-rich nuclei.

For β^+ -decay, a proton from the nucleus is converted to a neutron, a positron and an electron neutrino are emitted. This process generally happens in proton-rich nuclei. As positrons are antiparticles, they can not exist in the presence of matter.

As a result, the positron and an electron unite to a positronium, which decays to γ -quants (usually two). Due to the equivalence of energy and mass, the photons each have an energy that corresponds to the rest mass of the electron/positron, which is 511 keV. If the positronium decays into two photons, they are emitted at an angle of 180° due to the conservation of momentum.

Electron capture describes the interaction of a proton from the nucleus with an electron from the lowest energy shell, which are converted to a neutron and an electron neutrino. The hole in the lowest shell is filled by an electron from a higher shell, and the energy difference between the shells is emitted as a photon.

γ -decay After α - or β -decays, the resulting nucleus is usually left in a higher energy state. As it relaxes to its ground states, the energy is emitted in form of high energy photons, which are called γ -rays.

Auger Effect When an electron leaves the atom, the resulting hole is filled by an electron of a higher energy shell. The resulting excess energy might not be emitted as a photon, and instead can be transferred to another electron, which then leaves the nucleus. This electron is called Auger-electron.

Internal Conversion The excess energy resulting from a relaxing nucleus is not always emitted as a photon. It is also possible that the energy is absorbed by an electron in an atomic shell, which then has enough energy to leave the atom. The left over energy this electron has is the difference of the excess energy resulting from the relaxation and the

binding energy that the electron has to overcome in order to leave the atom. The space the electron leaves behind can be filled with an electron in a higher shell. The excess energy of this process can lead to X -rays or the emission of Auger electrons.

2.2 Decay schemes

In the following section we will discuss the decay schemes of the elements used in this experiment for calibration as well as the energy peaks we expect to detect.

The elements used in this experiment are ^{22}Na , ^{60}Co and ^{152}Eu .

Sodium ^{22}Na decays via β^+ -decay and electron capture. The β^+ -decay has a probability of 89.94%, the electron capture has a probability of 10.10%. The excited Neon atom resulting from the β^+ -decay relaxes into its ground state, due to which a peak of 1274 keV can be observed. Due to pair annihilation as a result of the β^+ -decay, another peak can be observed at 511 keV [1]. A simplified decay scheme of ^{22}Na is pictured in fig. 1.

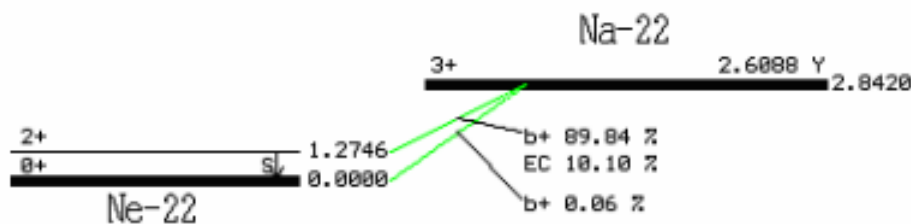


Figure 1: Simplified decay scheme of ^{22}Na . The transitions causing the two expected peaks at 1274 keV and 511 keV are pictured. Values and pictures are taken from [1]

Cobalt ^{60}Co decays via β^- -decay into a 4+ excited state of ^{60}Ni . The excited ^{60}Ni first relaxes into a 2+ excited state and then into its ground state. Observable peaks of the relaxation of ^{60}Ni are at 1273 keV and 1333 keV [1]. A simplified decay scheme of cobalt is pictured in fig. 2.

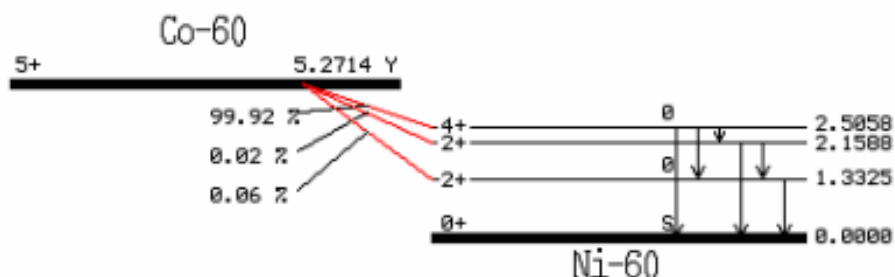


Figure 2: Simplified decay scheme of ^{60}Co . The peaks expected to be observed are the ^{60}Ni transitions of the energies 1273 keV and 1333 keV. Values and pictures are taken from [1].

Europium ^{152}Eu decays via β^+ -decay, β^- -decay and electron capture. A simplified version (adapted from [1]) of the decay scheme of ^{152}Eu is visible in fig. 3. The two highest peaks are of the energies 344 keV and 122 keV [1].

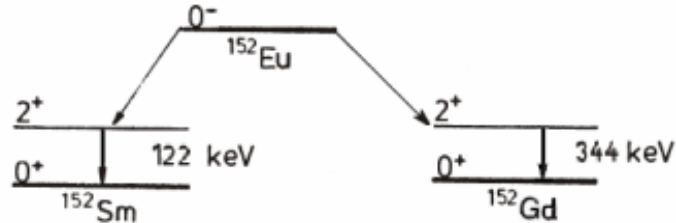


Figure 3: Simplified decay scheme of ^{152}Eu , taken from [1].

2.3 Interaction of Electromagnetic Radiation with Matter

Photoelectric Effect A photon transfers all of its energy to an electron of an atom, which then has enough energy to leave the atom. It is left with a kinetic energy of $E_{\text{kin}} = h\nu - E_{\text{bin}}$, where $h\nu$ is the energy of the photon and E_{bin} is the binding energy of the electron. In this process, the photon is completely absorbed by the electron. This is only possible with bound electrons, as the existence of the nucleus is necessary for the conservation of momentum. As the probability for the Photoelectric Effect is proportional to the fifth power of the nuclear charge number, this effect mainly occurs in heavy elements.

Compton Scattering Compton Scattering occurs when a photon and a free electron scatter. During this process, the photon transfers part of its energy to the electron and as a result experiences red shifting. The energy that the photon has after the interaction depends on the angle with which the scattering occurs.

Pair Creation If a photon has an energy of at least 1022 keV, it can transform all of its energy into a electron-positron-pair. The energy is converted to the rest mass of the electron and the positron (511 keV each).

3 Electronic Devices

In the following we will explain the devices used in this experiment. After discussing the scintillator and the photomultiplier, we will explain the different NIM-electronic components used to process the signal.

If not specified otherwise, the information in this section is taken from [2].

Scintillator A scintillator is a device used to detect ionizing particles. Passing the scintillator, the particles deposit energy due to the processes discussed in [section 2.3](#). This leaves the scintillator atoms in excited energy states. When the material used in the scintillator relaxes back into its ground state, it emits many low energy photons, which can be transformed to a measurable current using the photoelectric effect.

In general, two different types of scintillators are distinguished: Inorganic scintillators and organic scintillators.

Inorganic scintillators are doped semiconducting crystals. Their behavior can be explained using the band model of semiconductors. The incoming particles interact with the crystal, transferring their energy to the crystal. As a result, electrons are lifted from the valence band to the conduction band. When the electron relaxes back into the valence band, the excess energy is emitted as a photon. In a crystal which is not doped, this photon might have the same energy as the originally incoming particle. However, doping a crystal locally deforms the conduction band and creates additional energy levels an electron can occupy which are situated between the valence band and the conduction band. When the electron relaxes from this energy level to ground state, the energy of the emitted photon is not high enough to excite another electron. These photons can then reach the photomultiplier. Inorganic scintillators in general have a high density which leads to a relatively large amount of detectable photons and leads to a good resolution in the measurement of the energy of the original signal. However, the scintillation decay time is rather large, which means the resolution in time is not very good.

In organic scintillators, a signal is produced by using molecular transitions. The incoming photons excite a molecule, which then emits photons of measurable energy due to vibrational transitions. As vibrational transitions have a duration of only a few nanoseconds, organic scintillators are often used to measure the precise timing of a signal. However, the energy needed to excite the molecule is rather high, which leads to a lower resolution in the energy.

Photomultiplier As the signal produced by a scintillator is very weak, usually a photomultiplier is used to convert it into a measurable current. An optical fiber transfers the photons produced by the scintillator directly onto a photocathode, where the photons are absorbed and electrons are emitted via the photoelectric effect. These primary electrons are then accelerated by an electric field and hit a dynode. Several dynodes are placed after each other and arranged in a way that leads to very little loss of electrons between the dynodes. At the first dynode, the impact of each primary electron leads to the emission of secondary electrons. The number of secondary electrons depends on the applied voltage and often lies between a factor of 3 and 10. All electrons are then accelerated to the next dynode. As each dynode is held at a higher potential than the previous one, the process repeats, so that at the end a larger signal which is proportional to the size of the original signal is produced. Effectively, the photomultiplier converts the light signal from the scintillator to a measurable electrical signal.

Preamplifier The signals created by the photomultiplier are weak current signals, which are irregular in shape and hard to analyze. The preamplifier serves the purpose of transforming these signals into voltage pulses with an amplitude proportional to the incoming current. To do so, it integrates the incoming current over a predefined period of time. To minimize the noise on the weak signal from the photomultiplier, the preamplifier is located directly behind the photomultiplier. The outgoing voltage pulse has the characteristic form of a negative exponential signal with a long tail.

Main Amplifier The main amplifier is located behind the preamplifier and serves two purposes.

For one, it is used to change the pulse shape. This is done by specifying a shaping time between $0.5\ \mu\text{s}$ and $1.5\ \mu\text{s}$. The amplifier determines the maximum amplitude within the shaping time, which is then used to generate the outgoing signal. Cutting of the signal after the shaping time is done to prevent later signals from overlapping with the long decay time of the earlier signal, which would then lead to the registration of only one signal with a false value for the amplitude. It is important to ensure that the maximum amplitude is reached within the shaping time. However, long shaping times lead to long dead times in which new signals can not be detected, thus limiting the detectable frequency of signals. The other purpose of the main amplifier is to amplify the signal. This is done by adjusting the gain and the coarse gain settings.

There are two outputs of the main amplifier: a unipolar and a bipolar signal. As the energy of the original signal is proportional to the amplitude, the unipolar signal should be chosen if determining the energy is the main goal. However, if the main interest lies in the timing of the signal, it is advantageous to use the bipolar signal instead because its zero-crossing can easily be determined.

Single Channel Analyzer A single channel analyzer sorts the incoming signals by amplitude, which is proportional to the energy of the original signal. It is possible to select an energy range for the signal by adjusting the upper and lower level. If the incoming signal has an amplitude in the selected range, the single channel analyzer outputs a logical signal. There is a positive and a negative output. The positive output gives a square wave signal while the negative output generates a short negative pulse for usage with the timing unit. If the amplitude of the incoming signal is not in the selected range, there is no output. It is also possible to specify a delay with which the signal is generated.

Multi Channel Analyzer A multi channel analyzer sorts incoming signals by amplitude into channels. The channels then contain the number of signals with the corresponding amplitude. The multi channel analyzer is connected to a computer. Suitable software can be used to evaluate and illustrate the spectrum and save the count rates to a file. After an energy calibration it is possible to assign the channel numbers to the corresponding energies.

Linear Gate A linear gate is an electronic module which outputs an incoming signal only if it registers an enable signal. It can be used to analyze signals within a specific

energy range. To do so, it can be connected to the main amplifier and use the single channel analyzer output as an enable signal. The linear gate will then pass on the signal only if it is within the energy range specified at the single channel analyzer and block it otherwise.

Timing Unit A timing unit is used to convert a negative logical signal to a rectangular signal. It is also possible to specify the width and the polarity of the output signal. For example, it can be used to shape a signal from a single channel analyzer.

Coincidence Unit The coincidence unit checks whether two incoming logical signals are simultaneous. The incoming signals do not have to be perfectly aligned, instead, a positive logical rectangular signal is generated at the moment of the incoming signals overlap.

Hex Counter A hex counter can count logical signals within a specified period of time. For example, it counts the signals that are output by the coincidence unit, raising the hex counter by one every time a signal is registered.

4 Setup and Execution of the Experiment

4.1 Part 1: Evaluation of the Thorium Spectrum

The goal of the first part of the experiment is evaluating the spectrum of thorium. To do this, an inorganic NaI-crystal scintillator is used. The electrical circuit, built using the devices explained in [section 3](#) is depicted in [fig. 4](#).

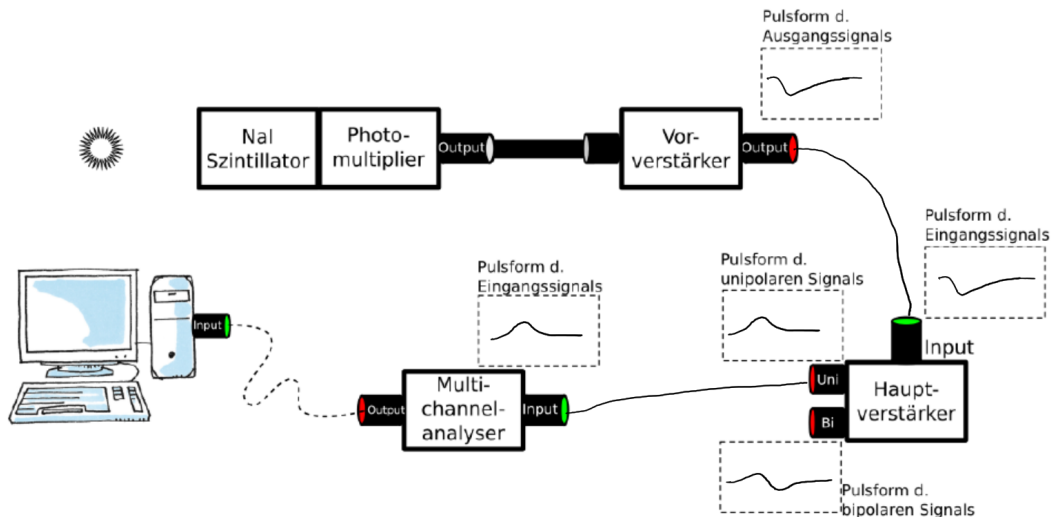


Figure 4: Electrical circuit for the measurement of the thorium spectrum, taken from the instruction [\[3\]](#). The expected shape of the output of each device is also depicted.

At first, the ^{22}Na probe was placed in front of the NaI scintillator. The scintillator preamplifier was then connected to the oscilloscope. To avoid reflection of the signal at the oscilloscope, a feedback resistor was added to each input. The observed signal has the expected shape (explained in [section 3](#)) and is depicted in [fig. 5](#).

Then, the preamplifier was connected to the main amplifier, and the oscilloscope was connected first to the unipolar, then to the bipolar output. The resulting graphs can be seen in [fig. 6](#) and [fig. 7](#), respectively. Using the oscilloscope, the rising time of the signal was roughly estimated to be around $1.3\ \mu\text{s}$. Therefore, the shaping time at the main amplifier was set to the closest possible value, which was $1\ \mu\text{s}$.

Next, the unipolar output of the main amplifier was connected to the multi channel analyzer. The software `Gamma Aquisition & Analysis` was used to depict the spectrum on the computer monitor. The expected peaks of ^{22}Na at 511 keV and 1274 keV were clearly visible. The observed spectrum is depicted in [fig. 16](#).

Next, the amplification of the main amplifier was adjusted. The amplification set at the main amplifier determines the energy range that can be measured by the multi channel analyzer. The purpose of measuring the spectra of sodium, cobalt and europium is to calibrate the energy of the multi channel analyzer. This means that the amplification settings should be set once and not be changed during the course of this experiment.



Figure 5: The ^{22}Na -signal detected by the NaI scintillator as given out by the preamplifier. The expected exponential shape is clearly visible.



Figure 6: The ^{22}Na -signal detected by the NaI scintillator as given out by the unipolar output of the main amplifier. The coarse gain was set to 20 and the gain to 2, which results in an amplification factor of 14.

As the goal of this experiment is to analyze the spectrum of thorium, the energy range detectable by the multi channel analyzer should contain all thorium peaks expected to be measured. The highest expected thorium peak has an energy of about 2700 keV. To make sure that it is in the detectable range, a rough estimate of this peaks location was made using the positions of the visible ^{22}Na peaks and the coarse gain and gain settings at the main amplifier were adjusted accordingly. In the end, the coarse gain was set to 20 and the gain was set to 2. As the gain setting had a scale from 0 to 10 which corresponds to



Figure 7: The ^{22}Na -signal detected by the NaI scintillator as given out by the bipolar output of the main amplifier. The coarse gain was set to 20 and the gain to 2, which results in an amplification factor of 14.

an amplification of 0.5 to 1.5, the effective amplification caused by the gain setting was 0.7, which puts the effective overall amplification to $20 \cdot 0.7 = 14$.

At this point, the multi channel analyzer was set to the maximum of 16 480 bins. With these settings, the ^{22}Na peaks were approximately located at channels 2800 and 6900 which put the expected channel number of the highest thorium peak at a clearly measurable 14 000 to 15 000, while at the same time minimizing the range in which nothing was expected to be measured.

After adjusting the gain, the amount of bins was selected. A higher amount of bins leads to a better energy resolution. However, a higher amount of bins also means that the number of counts registered per bin in a specific time frame is lower. As counting rates follow a poisson distribution, the error is calculated by taking the square root of the number of events. This means that for a higher amount of bins the relative error increases.

The sodium sample was to be measured over a time frame of approximately 30 min. To estimate the relative errors, a measurement of about 5 min was conducted. To reach a relative uncertainty of under 2% for the largest sodium peak, the amount of 8190 bins was selected. This results in a relative uncertainty of approximately 5% for the smaller peak.

After setting up the experiment as described above, the measurements were carried out. As planned beforehand, sodium was measured for 1790.342s which roughly corresponds to 30 min. After saving the spectrum calculated by the multi channel analyzer, the other elements were placed in turn before the scintillator and the measurement was started again. To reach a comparable relative error to the sodium measurement on the highest peaks, the time frames for the other elements were adjusted. The measurement time for

cobalt and europium were 2450.364 s and 3660.884 s, respectively. Then, the underground radiation was measured by recording the count rates over a time frame of 17477.029 s without placing anything in front of the scintillator. Finally, a measurement of thorium was conducted. As the count rates of thorium were expected to be relatively low, this measurement was taken over night, reaching a time frame of 51291.394 s.

The resulting spectra are depicted in [figs. 16 to 18, 20 and 21](#).

4.2 Part 2: Angle Dependency of Pair Annihilation

In the second part of the experiment the coincidence method is used to measure the angle dependency of pair annihilation. To do so, in addition of the NaI scintillator an organic plastic scintillator is necessary. For this part of the experiment, the isotope ^{22}Na is used.

The electrical circuit, using the devices explained in [section 3](#), is depicted in [fig. 8](#).

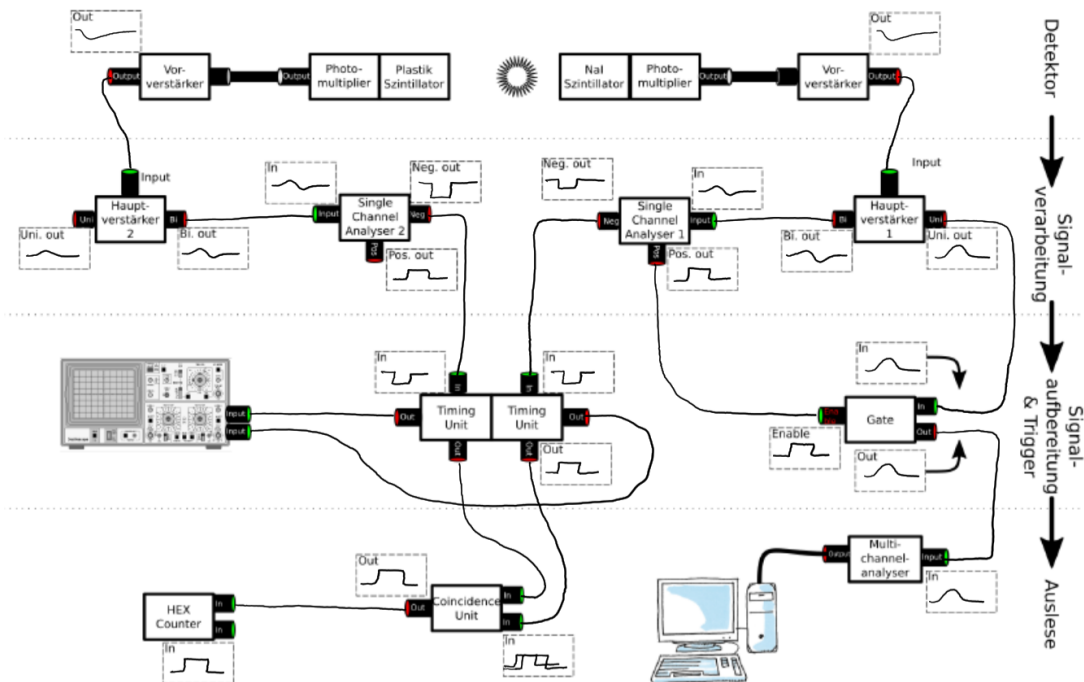


Figure 8: Electrical circuit for measuring the angle dependency of pair annihilation resulting from β^+ -decay of ^{22}Na . The expected shape of the signal is depicted at each output.

First, the sodium probe was placed before the NaI scintillator. Then, the preamplifier was connected to the amplifier. The amplifier settings for the shaping time, coarse gain and gain were not changed. Next, the bipolar output of the amplifier was connected to the single channel analyzer and the unipolar output was used as an input for the linear gate. The positive single channel analyzer output was used as the enable signal for the linear gate. At first, the energy range at the single channel analyzer was set to the maximum range. Then, while observing the spectrum at the computer, the energy range was gradually restricted, until only the 511 keV peak was visible. This is the peak caused

by pair annihilation, which is to be observed in this part of the experiment. The resulting settings for the selected energy range were $E = 1.30$ and $\Delta E = 0.50$. The restricted spectrum is visible in [fig. 22](#).

Next, the plastic scintillator was turned on and the preamplifier of the plastic scintillator connected to the oscilloscope. As before, a feedback resistor was added to each input to the oscilloscope. The resulting graph is visible in [fig. 9](#).



Figure 9: The ^{22}Na detected by the plastic scintillator as given out by the preamplifier. The expected shape (described in [section 3](#)) is clearly visible.

As before with the NaI scintillator, the graph visible at the oscilloscope was used to estimate the rising time of the signal. In this case, the rising time was approximately 5 ns. As the lowest possible setting at the main amplifier for the shaping time was 0.5 μs , this setting was selected.

Next, the plastic scintillator preamplifier was connected to the plastic scintillator main amplifier. To observe the signals output by the main amplifier, the unipolar output and the bipolar output were in turn connected to the oscilloscope. The resulting graphs are depicted in [fig. 10](#) and [fig. 11](#), respectively. It is immediately noticeable that the unipolar output does not look like a unipolar signal. This indicates that there is probably a problem with the unipolar output. In this experiment however, this is not of concern as the unipolar output is not needed to complete the measurement.

Then, the unipolar output of the main amplifier of the plastic scintillator was connected to the single channel analyzer of the plastic scintillator. As done before with the NaI scintillator, the unipolar output was connected to the linear gate, which was then connected to the multi channel analyzer, using the signal from the single channel analyzer as enable. This was done to set the energy range of the single channel analyzer for the plastic scintillator.

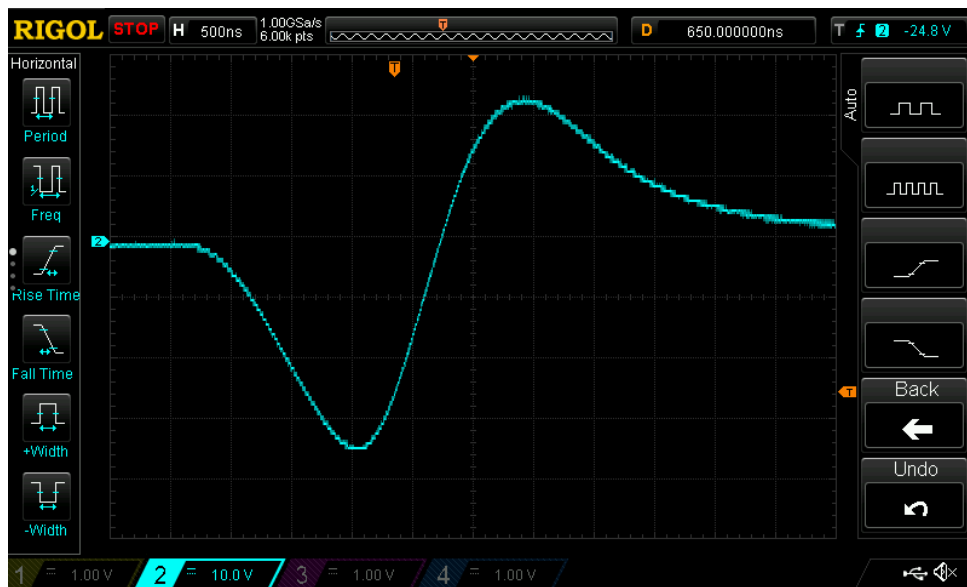


Figure 10: The ^{22}Na -signal measured by the plastic scintillator as given out by the unipolar output of the main amplifier. As the signal obviously does not look unipolar, there must be a problem with the unipolar output. This however is not of concern for this particular experiment.

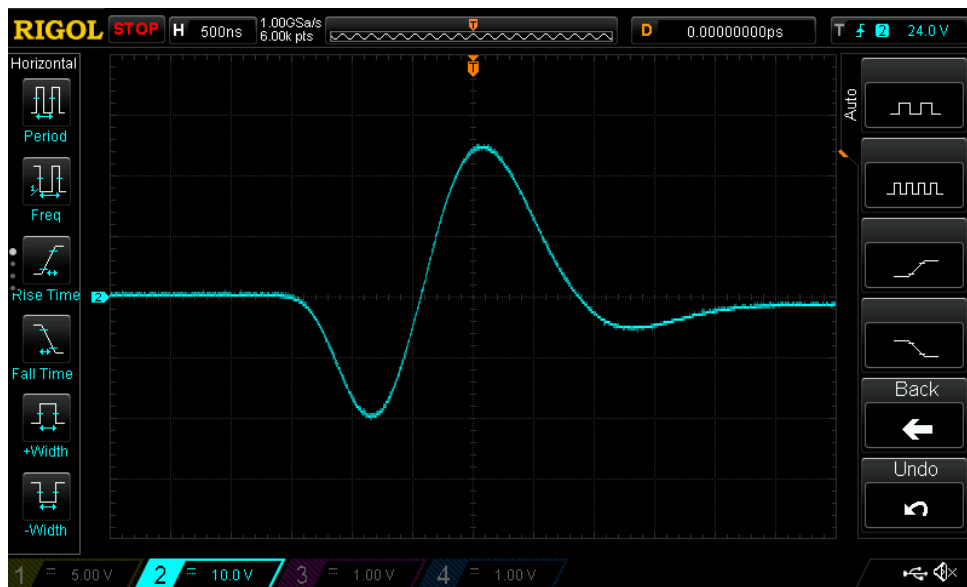


Figure 11: The ^{22}Na -signal measured by the plastic scintillator as given out by the bipolar output of the main amplifier.

It was not possible to see the expected ^{22}Na -peaks in the spectrum measured by the plastic scintillator. Therefore, the single channel analyzer energy settings were set to the maximum range, which was visually verified using the multi channel analyzer. After doing so, the linear gate was disconnected from the plastic scintillator main amplifier and single channel analyzer and reconnected to the NaI scintillator main amplifier and single channel analyzer.

As a next step, to verify the signals given out by the single channel analyzers, the negative output of both the plastic single channel analyzer were connected to the oscilloscope. The resulting graph can be seen in [fig. 12](#). As expected it shows a logical negative signal for each single channel analyzer.



Figure 12: The ^{22}Na -signal output of both the NaI scintillator single channel analyzer (yellow) and the plastic scintillator single channel analyzer (blue).

Then, the single channel analyzers were connected to timing units. The positive and negative timing unit output were once again connected to the oscilloscope, the resulting graphs can be seen in [fig. 13](#) and [fig. 14](#), respectively. It is easy to see that the negative signals coming from the single channel analyzers as depicted in [fig. 12](#) were converted to negative rectangular signals of equal width.

Next, the negative outputs of the timing units were connected to the coincidence unit. The positive outputs of the timing units as well as the output of the coincidence unit were connected to the oscilloscope.

The trigger was set to the signal provided by the NaI scintillator, as these are the signals that are selected by the NaI single channel analyzer and therefore exactly the 511 keV signals of interest. Using the oscilloscope, the frequency and placement of the plastic scintillator signals in comparison to the NaI scintillator signals were observed. In the plastic scintillator signals, a lot of noise (signals when the NaI scintillator did not provide a signal) could be observed. The signals did not perfectly align, as expected when taking statistical fluctuations into account. However, no systematic delay of one signal over the other was observable. Therefore, the delay that can be specified at the single channel analyzer was not changed, the settings remained at the preset 0s for both scintillators.

To minimize cases in which the coincidence unit gives out a signal even though the incoming signals have only minimal overlap, the width of the signals from the timing unit was adjusted by turning a screw and reduced to about 2 μs each.

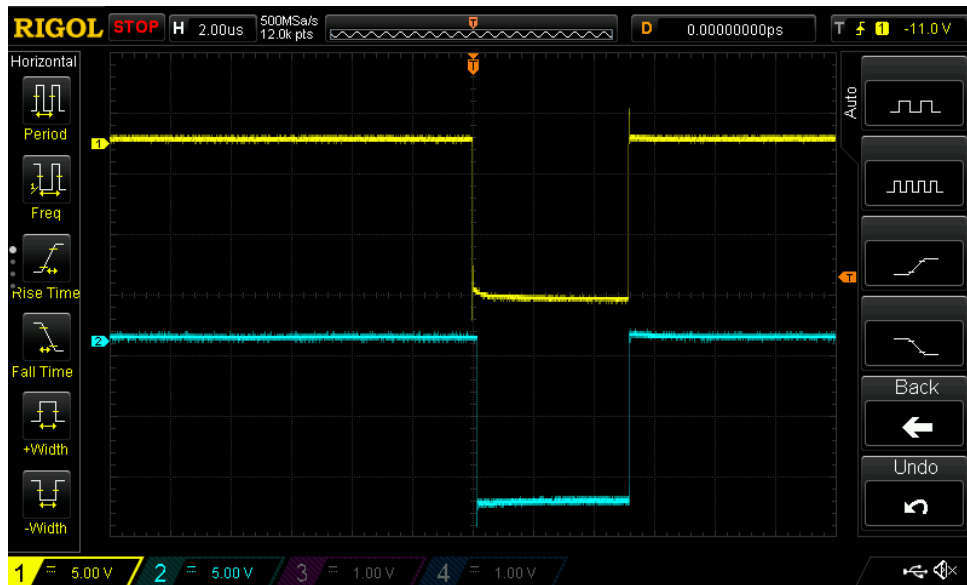


Figure 13: The ^{22}Na -signal measured by the NaI scintillator (yellow) and the plastic scintillator (blue), as given out by the positive outputs of the timing units. As the signal provided by the single channel analyzers is negative, the signals that can be observed here are also negative. This happens because using the positive timing channel unit outputs does not change the polarity of the signal.

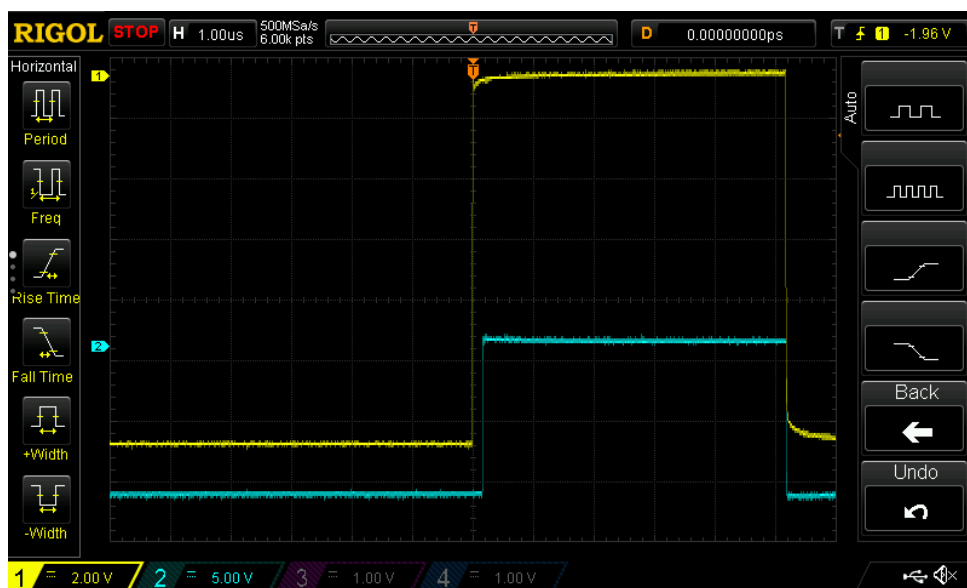


Figure 14: The ^{22}Na -signal measured by the NaI scintillator (yellow) and the plastic scintillator (blue), as given out by the negative outputs of the timing units. As the signal provided by the single channel analyzers is negative, the signals that can be observed here are positive. This happens because using the negative timing channel unit output changes the polarity of the signal.

The graph observable at the oscilloscope is pictured in [fig. 15](#). The signal from the NaI and plastic scintillators are yellow and blue, respectively. The signal provided by the coincidence unit is purple. It is easy to see that the coincidence unit provides a positive

signal as soon as the NaI and plastic scintillator signals overlap, but otherwise does not provide an output.

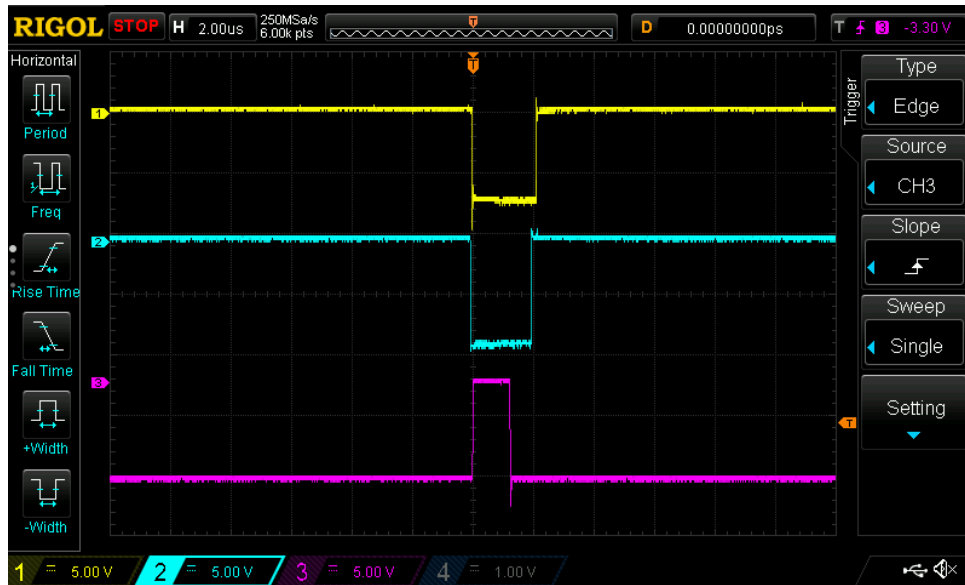


Figure 15: The ^{22}Na -signal given by the timing unit of the NaI scintillator (yellow) and the timing unit of the plastic scintillator (blue). The width of the signals set at the timing unit is $2\ \mu\text{s}$ each. The signal provided by the coincidence unit is depicted in purple. It is easy to see that the coincidence unit provides a positive signal as soon as the NaI and plastic scintillator signals overlap, but otherwise does not provide an output.

Finally, the output of the coincidence unit was connected to the hex counter. Next to the hex counter input a resistance was added to prevent signals from reflecting. As there was not enough time to conduct measurements over $1 \cdot 10^6\ \text{ms}$, which was the highest setting on the hex counter, for each angle setting of the plastic scintillator, the next highest setting was chosen. The measurements were carried out over $100 \cdot 10^3\ \text{ms}$, which corresponds to 100 s.

A test measurement was carried out with the plastic scintillator in a position of 0° on the scale, where the highest amount of counts was expected (the NaI scintillator was located at 180° to the plastic scintillator on this scale).

Then, the coarse gain and gain at the main amplifier of the plastic scintillator was adjusted. Higher values of coarse gain and gain guarantees all simultaneous signals of the NaI and the plastic scintillator to be recorded as such by the coincidence unit. This corresponds to a higher recorded count rate and leads to lower relative errors. However, higher values also drastically increase the noise of the plastic scintillator, which leads false hits. Using the oscilloscope to observe the noise, the coarse gain was adjusted to 500 and the gain to 6, leading to an effective amplification factor of 550. Short test measurements at various angles were also conducted to make sure that high count rates were measured around 0° , but almost no counts were registered at large angles of around 90° .

After completing the setup of the experiment the measurement was started. The plastic scintillator was turned to the most negative possible angle. This was -50° , as otherwise the end of the scintillator would have hit the wall. The hex counter was started for the time interval of 100 s, during which the signals received from the coincidence unit were counted. After the timer finished, the hex counter stopped counting, the number of signals was recorded in the lab notes and the plastic scintillator was moved by one indicator on the scale. The scale had indicators in 5° distances, and extra indicators in 1° distances were added between -10° and 10° . The 5° indicators were carved into the ground plate. Because the wheel of the scintillator arm fit very well into these carvings and a systematic uncertainty was not expected, the statistic uncertainty of these settings was estimated to 0.1° . The 1° indicators were only painted on top of the plate. Therefore the uncertainties were estimated bigger to 0.2° .

However, the noise on the plastic scintillator signal observed on the oscilloscope suddenly drastically increased, and it was not possible to measure anything but statistical fluctuations. After this became clear, the measurement was interrupted and the coarse gain and gain of the plastic scintillator main amplifier were readjusted. The readjusted value for the coarse gain was 50 and for the gain 6, resulting in an amplification factor of 55. Then the measurement was executed again as described above.

5 Data Analysis: Evaluation of the Thorium Spectrum

5.1 Energy calibration

To be able to compare the measured counting rates C'_{abs} , the counts have to be divided by the measurement time t to get the relative counting rate C' per second [cps]. Because the time measurement with the `Gamma Aquisition & Analysis` software was considered as exact, the relative counting rate and its uncertainty $\sigma_{C'}$ are given by

$$C' = \frac{C'_{\text{abs}}}{t} \quad \sigma_{C'} = \frac{\sigma_{C'_{\text{abs}}}}{t} = \frac{\sqrt{C'_{\text{abs}}}}{t}, \quad (5)$$

where $\sigma_{C'_{\text{abs}}} = \sqrt{C'_{\text{abs}}}$ due to the poisson distribution of each counting rate and t is the „Live time“ given by the software, considering the dead time of the scintillator.

To single out the decay counts C of each isotope, the underground counting rates were subtracted. As both values have statistic uncertainties, the combined uncertainty is given using the gaussian error propagation

$$C = C' - C'_{\text{underground}} \quad \sigma_C = \sqrt{(\sigma_{C'})^2 + (\sigma_{C'_{\text{underground}}})^2}. \quad (6)$$

The adjusted counting rates can be found in [figs. 16 to 18, 20 and 21](#).

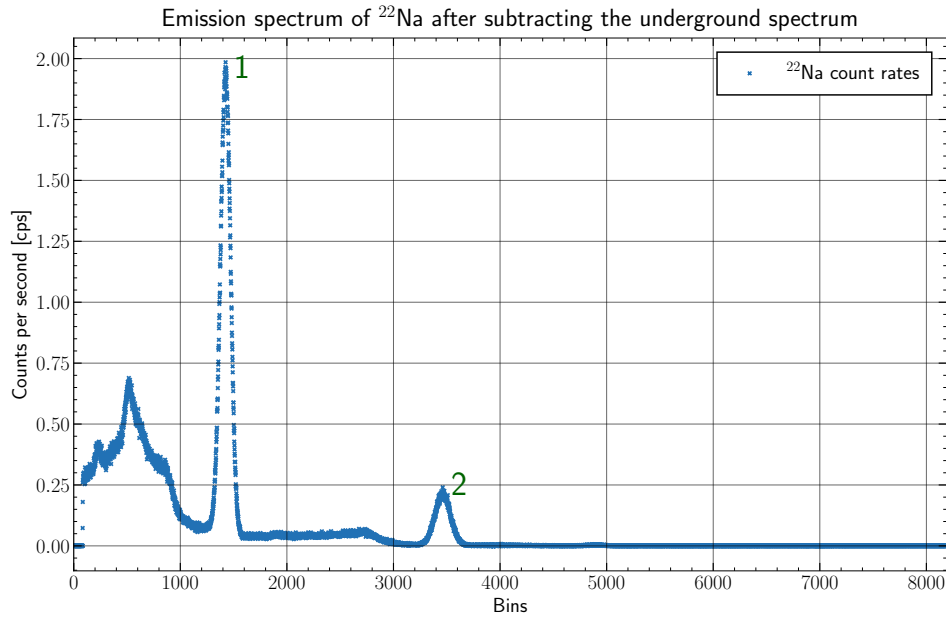


Figure 16: Full spectrum of ^{22}Na after subtracting of the underground spectrum (visible in [fig. 21](#)). The uncertainties are not shown to keep a clear output but are computed by [eqs. \(5\) and \(6\)](#). The numbers enumerate the peaks used for calibration. The corresponding gaussian fits can be found in [appendix A.2](#), the linear regression for energy calibration in [fig. 19](#).

The positions of the peaks were estimated by performing gaussian fits using

$$f(x|\mu, \sigma) = A \cdot \exp\left(\frac{(x - \mu)^2}{2\sigma^2}\right) \quad (7)$$

as the model function. The fits were performed in python, using `scipy.optimize.curve_fit`. The count-uncertainties were considered, using `absolute_sigma=True` to estimate the covariances out of the count-uncertainties and not out of the variations around the model function.

Close up views on each peak, with uncertainties, the values used for the fit and the optimal fit parameters can be found in [appendix A.2](#).

The estimated and expected positions B and energies E of the sodium peaks are listed in [table 1](#).

Peak	B	σ_B	E [keV]
1	1423.51	0.08	511.0
2	3462.0	0.3	1274.557

Table 1: Estimated positions and expected energies of the ^{22}Na Peaks. The bins were estimated using gaussian fits in python, close up views on the used data can be found in [appendix A.2](#). The expected energies are taken from [4].

With the same procedure, the peak positions of ^{60}Co and ^{152}Eu were estimated. The plots and data for cobalt can be found in [fig. 17](#) and [table 2](#) and for europium in [fig. 18](#) and [table 3](#).

Peak	B	σ_B	E [keV]
1	644.3	0.7	317.32
2	3187.0	0.3	1173.24
3	3612.0	0.3	1332.508

Table 2: Estimated positions and expected energies of the ^{60}Co Peaks. The bins were estimated using gaussian fits in python, close up views on the used data can be found in the [appendix appendix A.2](#). The expected energies are taken from [5].

In the ^{60}Co spectrum, a Compton edge and a Compton underground are well visible. The Compton edge can be seen approximately at bin position 2500. It describes the maximum amount of transferred energy from the incident photon to the electron during the Compton effect. The Compton underground can be seen for bins before the Compton edge. Here a constantly higher counting rate is measured without seeing distinct peaks.

With the estimated peak positions and the expected literature values for the energies, a linear conversion from bin number to the corresponding energy is possible. The linear correlation is expected due to the scintillator output signal, which is in theory proportional to the energy of the incoming particle.

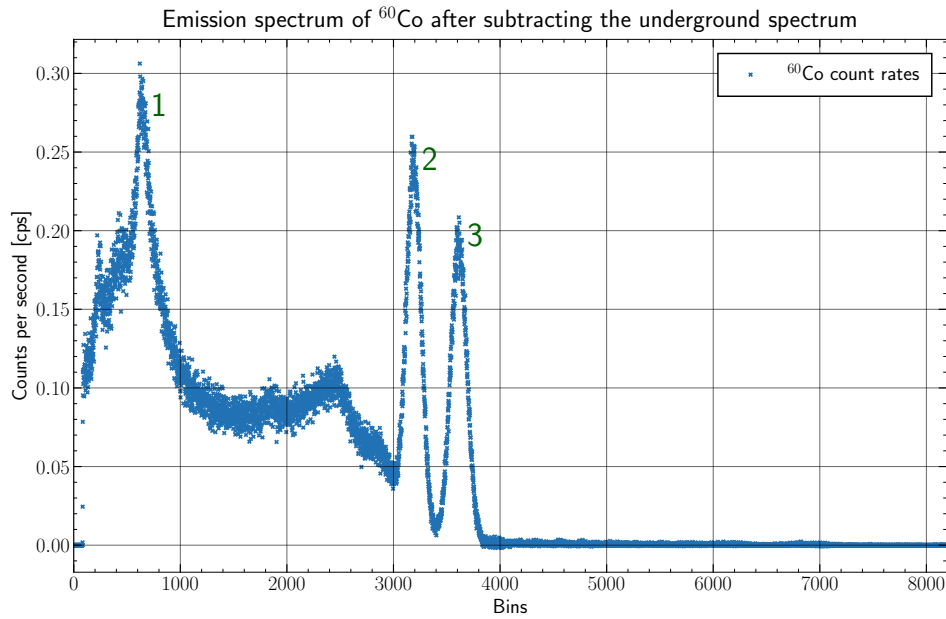


Figure 17: Full spectrum of ^{60}Co after subtracting of the underground spectrum (visible in [fig. 21](#)). The uncertainties are not shown to keep a clear output but are computed by [eqs. \(5\)](#) and [\(6\)](#). The numbers enumerate the peaks used for calibration. The corresponding gaussian fits can be found in [appendix A.2](#), the linear regression for energy calibration in [fig. 19](#).

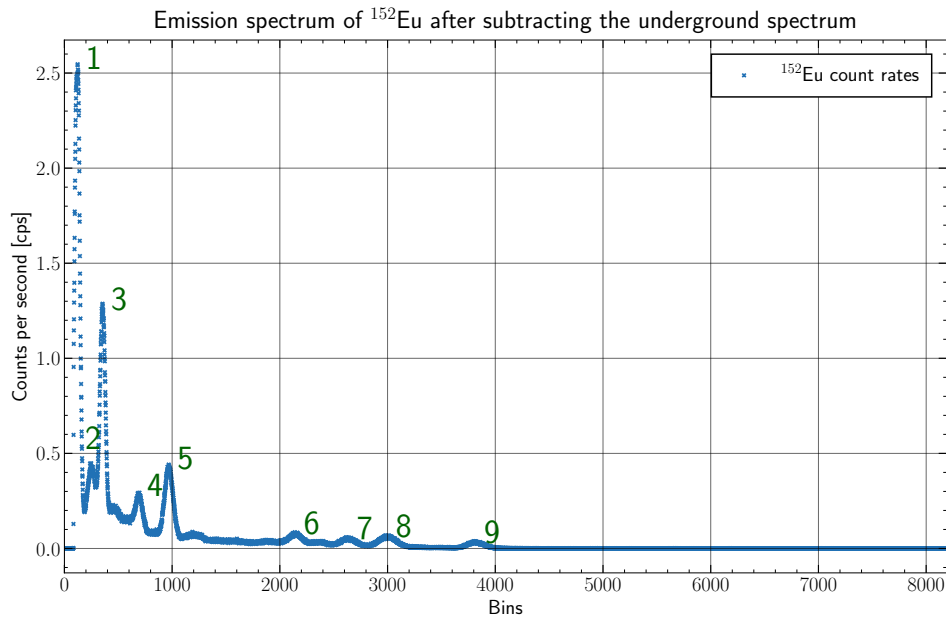


Figure 18: Full spectrum of ^{152}Eu after subtracting of the underground spectrum (visible in [fig. 21](#)). The uncertainties are not shown to keep a clear output but are computed by [eqs. \(5\)](#) and [\(6\)](#). The numbers enumerate the peaks used for calibration. The corresponding gaussian fits can be found in [appendix A.2](#), the linear regression for energy calibration in [fig. 19](#).

Peak	B	σ_B	E [keV]
1	118.93	0.05	121.7818
2	253.3	0.4	244.6976
3	354.29	0.07	344.2789
4	689.3	0.4	411.1171
5	968.82	0.15	443.996
6	2143.7	0.9	778.9066
7	2634.3	0.7	964.082
8	2997.5	0.6	1112.08
9	3815.7	0.7	1408.013

Table 3: Estimated positions and expected energies of the ^{152}Eu Peaks. The bins were estimated using gaussian fits in python, close up views on the used data can be found in [appendix A.2](#) The expected energies are taken from [6].

For the bin uncertainties, the uncertainties on the fit parameters were calculated from the covariance matrix.

In [fig. 19](#), the estimated peak positions are plotted against the expected energies. Because the literature values of the energies are considered as exact, the energy is shown on the x-axis to consider the y-uncertainties of the peak positions in the fit.

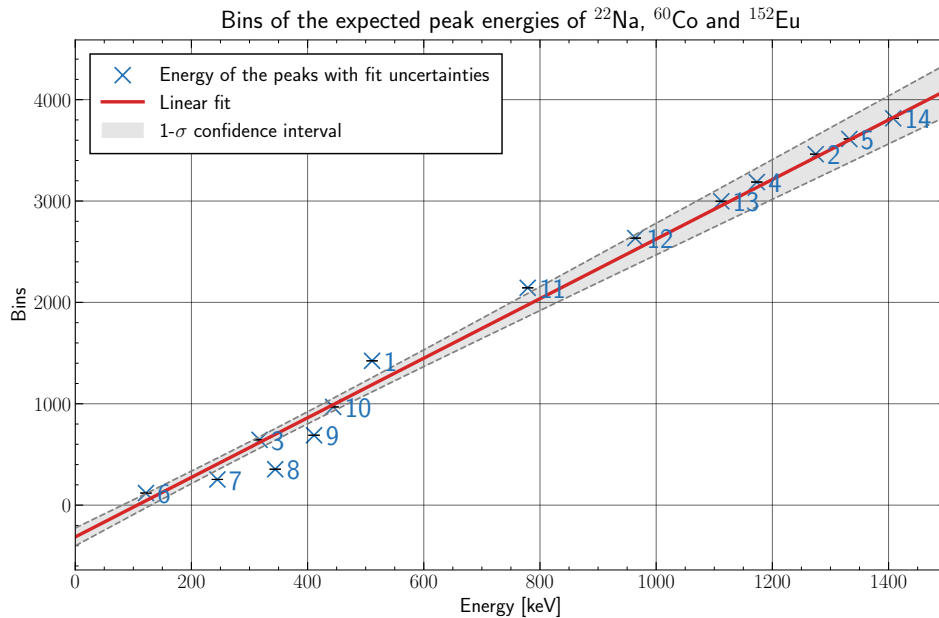


Figure 19: Linear regression to convert the bins to their corresponding energy. The spectra of ^{22}Na (number 1-2), ^{60}Co (number 3-5) and ^{152}Eu (number 5-14) were used for the fit, together with the expected energies from [4–6]. The linear regression was made using the fluctuations of the values around the model function, to get an appropriate confidence interval. The equations and values can be found in [eqs. \(8\) and \(9\)](#).

The linear regression was performed using `scipy.optimize.curve_fit` with the option `absolute_sigma=False` to calculate the covariance matrix from the fluctuations of the values around the model function. This allows to estimate an appropriate confidence interval.

For the fit, a linear function of the form

$$f(x) = a + b \cdot x \quad (8)$$

was used. The the optimal parameters resulting from the fit were

$$a = -310 \pm 90 \quad (8a)$$

$$b = (2.9 \pm 0.2) \text{ keV}^{-1}. \quad (8b)$$

With this information, a conversion from the peaks bin number to the corresponding energy is possible. The uncertainty is calculated using gaussian error propagation and is given by

$$E(B) = \frac{B - a}{b} \quad \sigma_{E(B)} = \sqrt{\left(\frac{1}{b}\sigma_B\right)^2 + \left(\frac{1}{b}\sigma_a\right)^2 + \left(\frac{B - a}{b^2}\sigma_b\right)^2} \quad (9)$$

5.2 Examination of the ^{228}Th spectrum

Using the calibration above, the other spectra can now be interpreted. First, the peaks of the ^{228}Th spectrum are examined.

The ^{228}Th spectrum after subtraction of the underground spectrum is visible in [fig. 20](#). Here, 9 peaks were evaluated. The close up views and detailed fit information are shown in [appendix A.2](#). For a clearer view of the smaller peaks, a plot with logarithmic y -scale can be found in [fig. 24](#).

The peak positions that were estimated using gaussian fits are listed in [table 4](#). The corresponding energies and uncertainties were calculated using [eq. \(9\)](#).

5.3 Examination of the underground spectrum

In the underground spectrum, apart from the expected underground noise a clear peak is visible. This peak will also be examined. The full underground spectrum is shown in [fig. 21](#).

With the above energy calibration, the energy of the peak can be calculated. It is listed in [table 5](#).

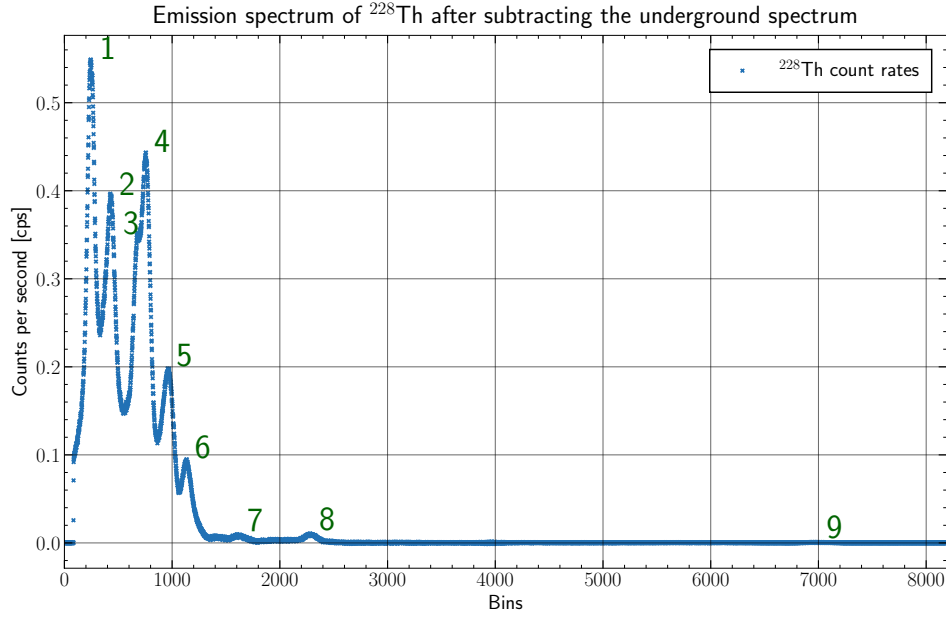


Figure 20: Full spectrum of ^{228}Th after subtracting of the underground spectrum (visible in [fig. 21](#)). The uncertainties are not shown to keep a clear output but are computed by [eqs. \(5\)](#) and [\(6\)](#). The numbers enumerate the evaluated peaks. The corresponding gaussian fits can be found in [appendix A.2](#), the calculated energies in [table 4](#). A plot with logarithmic y scale, in which the last peak is more easily distinguishable, can be found in [fig. 24](#).

Peak	B	σ_B	E [keV]	σ_E [keV]
1	247.98	0.07	190	30
2	428.7	0.2	250	40
3	685.8	0.8	340	40
4	753.12	0.15	360	40
5	961.9	0.3	430	40
6	1130.9	0.3	490	50
7	1616.7	1.6	660	60
8	2284.9	0.7	880	70
9	6995.0	4.0	2490	180

Table 4: Estimated positions and calculated energies of the ^{228}Th Peaks. The bins were estimated using gaussian fits in python, close up views on the used data can be found in [appendix A.2](#). The energies were calculated using the linear regression in [eq. \(9\)](#). The uncertainties were calculated by gaussian error propagation.

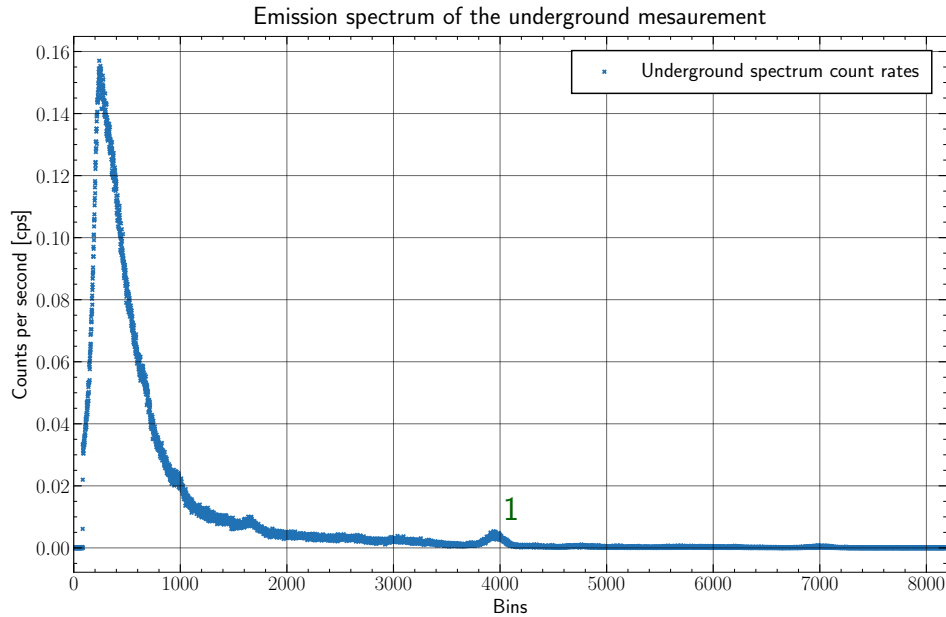


Figure 21: Full underground spectrum. The uncertainties are not shown to keep a clear output but are computed by eqs. (5) and (6). The number enumerates the evaluated peak. The corresponding gaussian fit can be found in appendix A.2, the calculated energy in table 5.

Peak	B	σ_B	E [keV]	σ_E [keV]
1	3950.5	1.1	1450	110

Table 5: Estimated positions and calculated energies of the Peaks in the underground spectrum. The bin was estimated using a gaussian fit in python, a close up view of the used data can be found in appendix A.2. The energy was calculated using the linear regression in eq. (9). The uncertainty was calculated by gaussian error propagation.

5.4 Interpretation of the ^{228}Th spectrum

Now that the energies of the peaks are calculated, the spectrum can be interpreted. To find possible transitions we compare the calculated energies to those of known transitions in the ^{228}Th decay scheme. The transition energies are taken from [7–13].

Peak 1: (appendix A.2) Due to the relatively high amplitude of the decay peak, it is most probably caused by the decay of $^{228}\text{Th} \rightarrow ^{224}\text{Ra}$. This decay is expected at an energy of 84.373 keV, which is smaller than the calculated energy of (190 ± 30) keV. The deviation will be mentioned in the discussion later.

Peak 2: (appendix A.2) The lower second peak at (250 ± 40) keV most probably results from the decay of $^{212}\text{Pb} \rightarrow ^{212}\text{Bi}$ with an energy of 115.183 keV. Again an offset to the calculated energy is well visible.

Peak 3 and 4: ([appendix A.2](#)) Peak 3 and 4 have a high overlap. It is to be expected that the corresponding decay transitions have energies lying very close to each other. This is the case for the decay of $^{212}\text{Pb} \rightarrow ^{212}\text{Bi}$ with an energy of 238.632 keV and $^{224}\text{Ra} \rightarrow ^{220}\text{Rn}$ with an energy of 240.986 keV. These two decays are the most probable to correspond to the visible peaks at calculated energies of (340 ± 40) keV and (360 ± 40) keV.

Peak 5: ([appendix A.2](#)) Considering the previous offsets, this peak is most likely to result from the decay of $^{212}\text{Pb} \rightarrow ^{212}\text{Bi}$ at 300.09 keV. The calculated energy is again higher at (430 ± 40) keV.

Peak 6: ([appendix A.2](#)) Due to its relatively high amplitude, this peak most likely results from superposition of multiple minor decays. The major contributions probably result from $^{224}\text{Ra} \rightarrow ^{220}\text{Rn}$ with an energy of 422.04 keV and the decay of $^{212}\text{Pb} \rightarrow ^{212}\text{Bi}$ at 415.27 keV. The calculated energy of the peak lies at (490 ± 50) keV.

Peak 7: ([appendix A.2](#)) This low amplitude peak is calculated to an energy of (660 ± 60) keV and most probably results from the decay of $^{208}\text{Tl} \rightarrow ^{208}\text{Pb}$ at 583.187 keV.

Peak 8: ([appendix A.2](#)) The energy of this peak has been estimated to (880 ± 70) keV. Considering its amplitude, the peak is most probably measured due to the decay of $^{208}\text{Tl} \rightarrow ^{208}\text{Pb}$ at 860.56 keV.

Peak 9: ([appendix A.2](#)) This is the peak we expected to see at a high channel, to which we adjusted the gain of the NaI scintillator main amplifier. The calculated energy is (2490 ± 180) keV. It almost certainly corresponds to the decay from $^{208}\text{Tl} \rightarrow ^{208}\text{Pb}$ with an energy of 2614.511 keV. It is noticeable that now the calculated energy is smaller than the peak energy. This effect will be discussed later.

5.5 Interpretation of the underground spectrum

One clear peak is visible in the underground spectrum ([appendix A.2](#)), even though no radioactive probe was held near to the scintillator. Considering its calculated energy of (1450 ± 110) keV, this signal results most probably from the decay of ^{40}K which occurs often in nature so that it is also probable to be found in the experiment room. ^{40}K decays to an excited state of ^{40}Ar which then emits γ -radiation at an energy of 1460.81 keV [14].

6 Data Analysis: Angle Dependency of Pair Annihilation

6.1 Coincidence measurement

To correctly adjust the energy interval at the single channel analyzer to measure only the first ^{22}Na peak, the spectrum was recorded again for a short time period. The result is visible in [fig. 22](#).

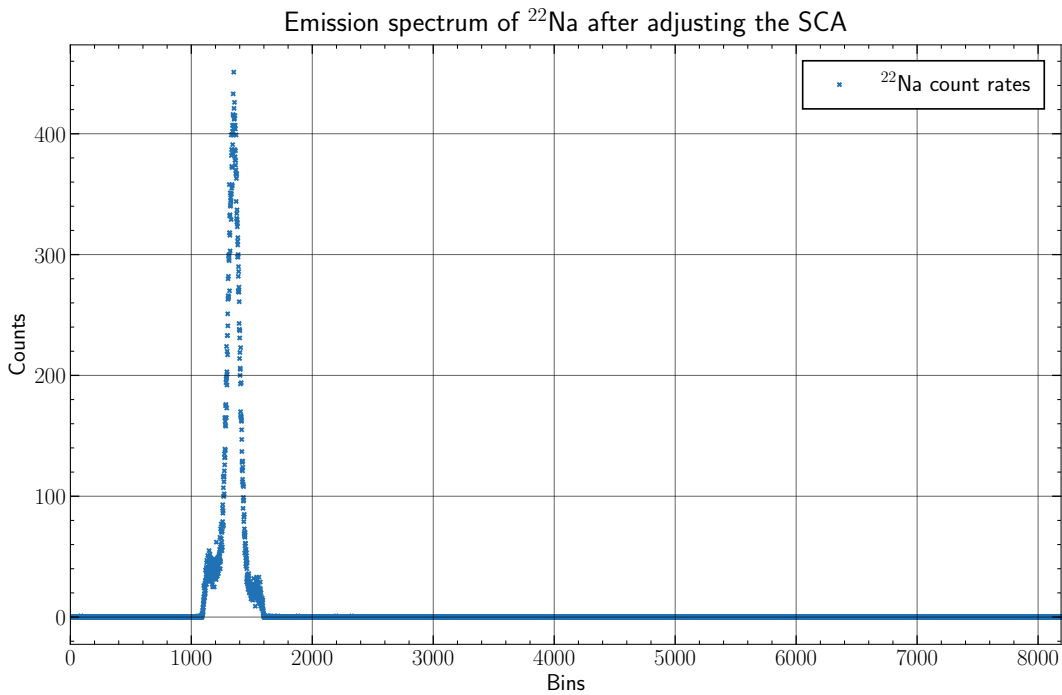


Figure 22: ^{22}Na spectrum after adjusting the energy interval to the first ^{22}Na peak. This guarantees that only signals within this energy range will trigger a signal for the coincidence measurement.

The counting rates for a set time interval of 100 s from the Hex counter as well as the angles with the corresponding uncertainties can be taken from the lab notes in [appendix A.3](#). The uncertainties of the counting rates can be computed using $\sigma_{C'} = \sqrt{C'}$ due to the statistic Poisson distribution of the counts.

As we expect no coincidence signal at the angle of 90° , the counts measured at this angle must result exclusively from statistic noises. To prevent these from distorting the measurement, the counting rate at 90° was subtracted from each value. The combined uncertainties result from a gaussian error propagation are calculated by

$$C = C' - C'_{90} \quad \sigma_C = \sqrt{(\sigma_{C'})^2 + (\sigma_{C'_{90}})^2}. \quad (10)$$

The adjusted counting rates are plotted against the corresponding angle in [fig. 23](#).

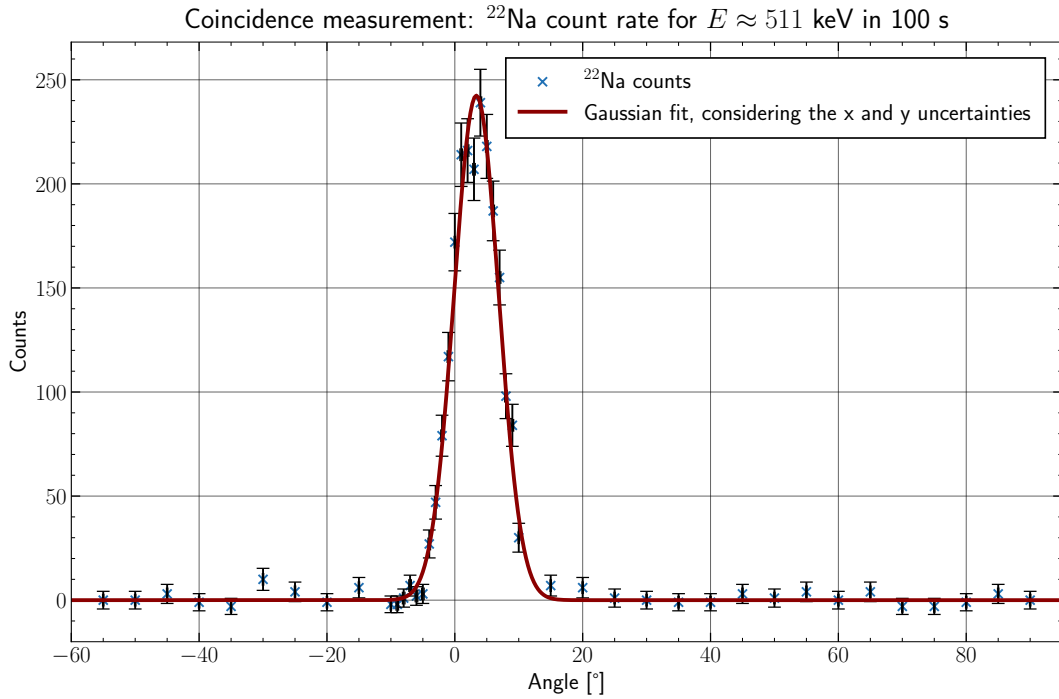


Figure 23: Coincidence measurement counting rates with x- and y-uncertainties plotted against the angle of the plastic scintillator. 0° corresponds to an angle of 180° between the two scintillators. Therefore a maximum of the counting rate is expected at 0° due to the conservation of momentum in the positronium decay. The gaussian fit (Model: eq. (7)) was performed considering the x-uncertainties as well as the y-uncertainties. The optimal fit parameters can be found in eq. (11).

The gaussian fit (Model: eq. (7)) was performed in python using `scipy.odr`. This allows to consider the uncertainties of the counting rates as well as the uncertainties of the angle measurement. The optimal fit parameters are

$$\begin{aligned} A &= (240 \pm 7) \\ \mu &= (3.37 \pm 0.11)^\circ \\ \sigma &= (3.49 \pm 0.09)^\circ. \end{aligned} \tag{11}$$

The reduced χ^2 value of the fit is

$$\chi_\nu^2 = 0.886, \tag{12}$$

which speaks for a high goodness of the fit.

As already anticipated during the measurement, it can be seen that the maximum position of the peak is shifted towards the positive angles. The maximum occurs at $(3.37 \pm 0.11)^\circ$. This could indicate systematic deviation which will be discussed in the following section.

7 Summary and Discussion

7.1 Thorium Spectrum

Using gaussian fits to estimate the peak positions of the known energy peaks in the spectra of ^{22}Na , ^{60}Co and ^{152}Eu , an energy calibration was performed. The peak energies were taken from [4–6] and are plotted in [fig. 19](#) against the corresponding bins. The expected linear relation between the two values was used to perform a linear fit. As a result, the corresponding energy to a bin can be calculated using the formula [eq. \(9\)](#).

It is noticeable that the resulting fit has a large negative y-axis offset. This was not expected because an ionizing particle with 0 keV energy should not dispose any energy, especially not negative energy, in the scintillator. However, this effect can probably be explained with the fact that the theoretical linear relation between the energy of the incoming particle and the amplitude of the output signal is just an approximation. Another important fact is that for all the taken measurements, counting rates of the first ≈ 80 bins of the multi channel analyzer were constantly 0. This indicates a possible systematic deviation in the measurement.

Then, the calculated relation between bins and energy was used to analyze the spectra of the underground measurement and the ^{228}Th spectrum. As described in [section 5.4](#), the visible peaks of ^{228}Th were assigned to the most probable decay energies in the spectra of ^{228}Th and its decay products. It was noticeable that the energies calculated using the linear relation [eq. \(9\)](#) were mostly higher than the energies of the corresponding transitions. Only the energy of the last peak at (2490 ± 180) keV was lower than the expected peak energy.

This strongly indicates a systematic error originating from the calibration. As several peak positions used for the calibration lie beside the linear model function in [fig. 19](#), this is not very surprising. For a better result, the clearest calibration peak positions could have been weighted more strongly, so that for example the very well visible first peak of ^{22}Na could have had a higher contribution to the fit compared to other, smaller peaks, where the position was harder to estimate.

However, as the gaussian fit uncertainties were used as uncertainties of the maximums bin position, this was not possible. Another factor is that the uncertainties resulting from the fit are very small compared to the bin values, making a weighted linear regression even harder to perform. Another way the calibration fit could be improved is to use more isotopes with very well visible decay peaks and known energy transitions.

Additionally, longer measurements would allow for higher counting rates, leading to smaller relative uncertainties for the measured values. In this case, the contribution of underground noise, which definitely affected the goodness of fit for the smaller peaks, would also be reduced.

In the same way, the underground spectrum was evaluated. The only clearly visible peak in [fig. 21](#) was estimated to an energy of (1450 ± 110) keV. As the measurement was performed without a radioactive probe held in front of the scintillator, the peak must have occurred due to other radioactive decays in the room, e.g. from impurities in the concrete

of the walls. This suggests that the element responsible for this decay might often occur in nature. This is the case for ^{40}K . As the decay energy of $^{40}\text{K}\alpha$ matches the measured energy range, the decay peak could very likely emerge from this decay.

7.2 Coincidence Measurement

Using the coincidence method, the angle at which pair annihilation can be measured was determined to be

$$(3.37 \pm 0.11)^\circ.$$

This result differs by over 30 standard deviations from the expected value of 0° , which means the two values are not compatible.

A possible reason for the offset is the scale for the angle itself. The angles had to be measured using a large metal plate with markings for the angle. For every 5° there was a small carving in the plate, in which the wheel the plastic scintillator was balancing on could be placed. This prevented the plastic scintillator from moving during the measurement. However, there was no good way to verify the markings and carvings on the plate. This is true especially for the positions from -10° to 10° , which were lightly marked in pencil and had not been carved. Therefore, it is quite possible that the scintillator may have moved slightly while measuring.

It is however way more likely that the offset was caused by the placement of the components. For example, it is possible that the NaI scintillator was not perfectly placed at 180° . In this case, it is possible that the angle of the plastic scintillator at $(3.37 \pm 0.11)^\circ$ was actually at exactly 180° with respect to the NaI scintillator, which would cause the offset seen in the result. This possible systematic uncertainty is most likely to explain the observed offset.

Furthermore, it was not possible to place the ^{22}Na probe on the axis around which the plastic scintillator was rotated. Therefore, for different angles the probe was slightly displaced. This might have been enough to change the angle the plastic scintillator was located at with respect to the probe, which then of course means that the angles measured were not accurate.

A Appendix

List of Figures

1	Simplified decay scheme of ^{22}Na	3
2	Simplified decay scheme of ^{60}Co	3
3	Simplified decay scheme of ^{152}Eu	4
4	Circuit Part 1	8
5	NaI scintillator, Preamplifier	9
6	NaI scintillator, Main Amplifier, Unipolar Output	9
7	NaI scintillator, Main Amplifier, Bipolar Output	10
8	Circuit Part 2	11
9	Plastic Scintillator, Preamplifier	12
10	Plastic Scintillator, Main Amplifier, Unipolar Output	13
11	Plastic Scintillator, Main Amplifier, Bipolar Output	13
12	NaI scintillator, Single Channel Analyzer, Negative Output	14
13	NaI and Plastic Scintillator, Positive Timing Unit Output	15
14	NaI and Plastic Scintillator, Negative Timing Unit Output	15
15	NaI and Plastic Scintillator, Timing Unit Output with Coincidence Unit	16
16	Full spectrum of ^{22}Na	18
17	Full spectrum of ^{60}Co	20
18	Full spectrum of ^{152}Eu	20
19	Calibration of bins to energy	21
20	Full spectrum of ^{228}Th	23
21	Full underground spectrum	24
22	^{22}Na spectrum after adjusting the SCA	26
23	Coincidence measurement counting rates	27
24	Full spectrum of ^{228}Th with logarithmic y-scale	32

List of Tables

1	Positions and energies of the ^{22}Na Peaks	19
2	Positions and energies of the ^{60}Co Peaks	19
3	Positions and energies of the ^{152}Eu Peaks	21
4	Positions and energies of the ^{228}Th Peaks	23
5	Positions and energies of the Peaks in the underground spectrum	24

Bibliography

- [1] Tobias Kotyk, *Versuche zur radioaktivität im physikalischen fortgeschrittenen praktikum der albert-ludwigs-universität freiburg* (Institute of Physics, University of Freiburg, 2005, Aug. 15, 2022).
- [2] *Fortgeschrittenen praktikum teil i, szintillationszähler, theorie und geräte* (Institute of Physics, University of Freiburg, 2005, Aug. 15, 2022).
- [3] Th. Klapdor-Kleingrothaus, *Fortgeschrittenen praktikum teil i, szintillationszähler* (Institute of Physics, University of Freiburg, 2017, Aug. 15, 2022).
- [4] 2009 CIEMAT /M. Galan, *Bnm - lnhb/cea - table de radionucléides - 22na* (Aug. 2022).
- [5] 2012 INEEL /R. G. Helmer, *Bnm - lnhb/cea - table de radionucléides - 60co* (Aug. 17, 2022).
- [6] 2004 USP LBNL / V.R. Vanin / R.M. de Castro / E. Brouwne, *Bnm - lnhb/cea - table de radionucléides - 152eu* (Aug. 17, 2022).
- [7] 2004 IAEA / A.L. Nichols, *Bnm - lnhb/cea - table de radionucléides - 208tl* (Aug. 17, 2022).
- [8] 2004 IAEA / A.L. Nichols, *Bnm - lnhb/cea - table de radionucléides - 212bi* (Aug. 17, 2022).
- [9] 2004 IAEA / A.L. Nichols, *Bnm - lnhb/cea - table de radionucléides - 212pb* (Aug. 17, 2022).
- [10] 2004 IAEA / A.L. Nichols, *Bnm - lnhb/cea - table de radionucléides - 216po* (Aug. 17, 2022).
- [11] 2004 IAEA / A.L. Nichols, *Bnm - lnhb/cea - table de radionucléides - 220rn* (Aug. 17, 2022).
- [12] 2004 IAEA / A.L. Nichols, *Bnm - lnhb/cea - table de radionucléides - 224ra* (Aug. 17, 2022).
- [13] 2004 IAEA / A.L. Nichols, *Bnm - lnhb/cea - table de radionucléides - 228th* (Aug. 17, 2022).
- [14] *Kalium-40* (ld-didactic, Aug. 18, 2022), <https://www.ld-didactic.de/software/524221de/Content/Appendix/K40.htm>.
- [15] *Die zerfallskette des thorium-232* (ld-didactic, Aug. 18, 2022), <https://www.ld-didactic.de/software/524221de/Content/Appendix/Th232Series.htm>.
- [16] atlas.physics, *Compton edge* (ld-didactic, Aug. 18, 2022), http://atlas.physics.arizona.edu/~shupe/Physics_Courses/Phys_586_S2015_S2016_S2017/LectureSupplements/ComptonEdge.pdf.

A.1 Thorium Spectrum with Logarithmic y-scale

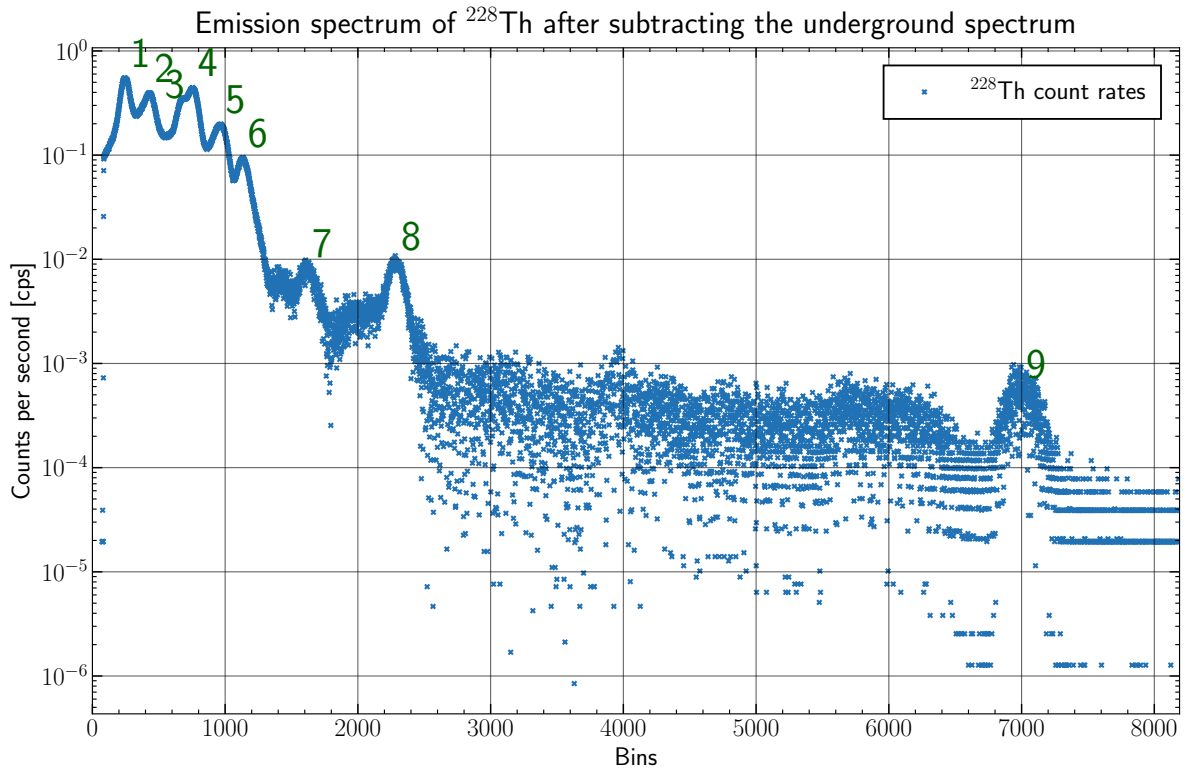
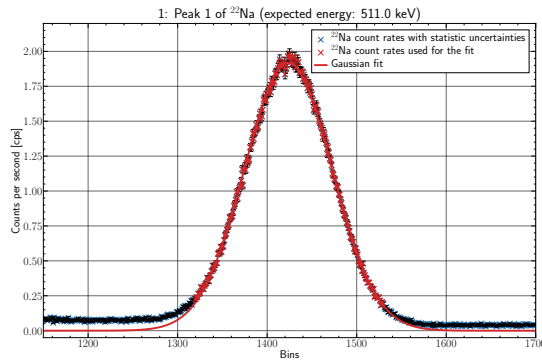


Figure 24: Full spectrum of ^{228}Th after subtracting of the underground spectrum (visible in [fig. 21](#)) depicted with a logarithmic y -scale. The uncertainties are not shown to keep a clear output but are computed by [eqs. \(5\)](#) and [\(6\)](#). The numbers enumerate the evaluated peaks. The corresponding gaussian fits can be found in [appendix A.2](#), the calculated energies in [table 4](#). A plot with linear y -scale can be found in [fig. 20](#).

A.2 Close up peaks

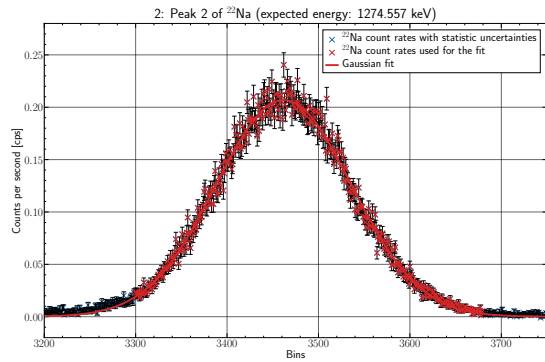
In the following, all peaks of the different spectra used for the energy calibration as well as the thorium peaks and underground measurement peaks used in the analysis are depicted separately. For each peak, the fit used to determine the peak position is also marked. The parameters of the fit as well as the reduced χ^2 value for the fit and the energy of the peak are listed in a table below each peak. For sodium, cobalt and europium the energies listed are literature values taken from the instructions [4–6]. The energies listed for the thorium and underground peaks are the energies determined by using the energy calibration eq. (9).

^{22}Na Peaks



1: Peak 1 of ^{22}Na (expected energy: 511.0 keV)			
A [cps]	1.921	\pm	0.004
μ	1423.51	\pm	0.08
σ	48.78	\pm	0.08
χ^2_ν	1.43		
E [keV]	511.0		

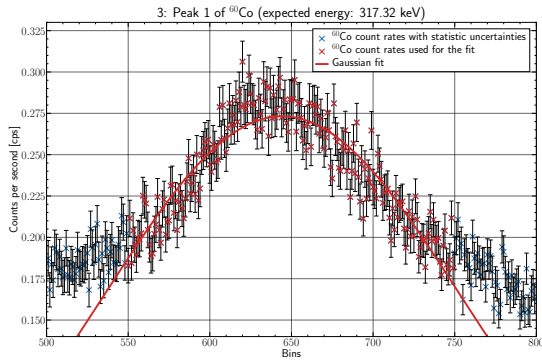
(a) Fit parameters, reduced χ -square test and expected energy for peak 1 of ^{22}Na .



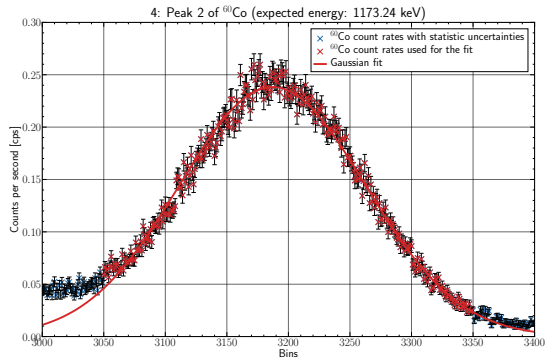
2: Peak 2 of ^{22}Na (expected energy: 1274.557 keV)			
A [cps]	0.2068	\pm	0.0010
μ	3462.0	\pm	0.3
σ	74.3	\pm	0.3
χ^2_ν	1.06		
E [keV]	1274.557		

(b) Fit parameters, reduced χ -square test and expected energy for peak 2 of ^{22}Na .

^{60}Co Peaks



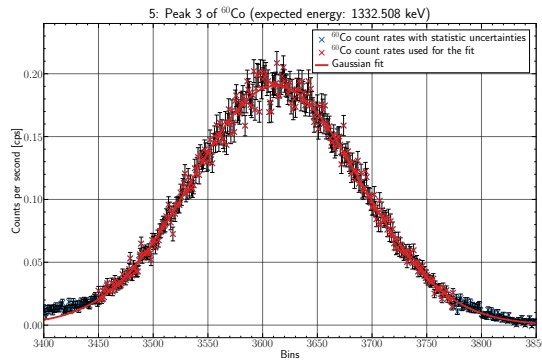
A [cps]	0.2732	\pm	0.0013
μ	644.3	\pm	0.7
σ	108.7	\pm	1.5
χ^2_ν	1.48		
E [keV]	317.32		



A [cps]	0.2383	\pm	0.0010
μ	3187.0	\pm	0.3
σ	75.6	\pm	0.3
χ^2_ν	1.38		
E [keV]	1173.24		

(a) Fit parameters, reduced χ -square test and expected energy for peak 1 of ^{60}Co .

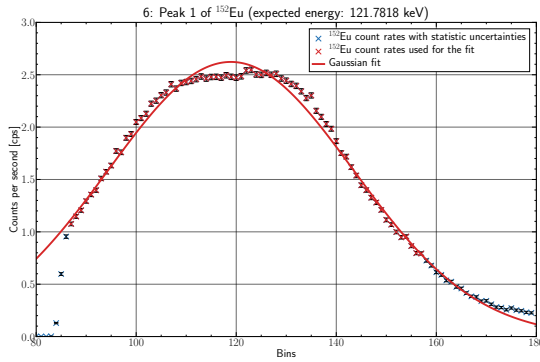
(b) Fit parameters, reduced χ -square test and expected energy for peak 2 of ^{60}Co .



A [cps]	0.1903	\pm	0.0008
μ	3612.0	\pm	0.3
σ	76.8	\pm	0.3
χ^2_ν	0.935		
E [keV]	1332.508		

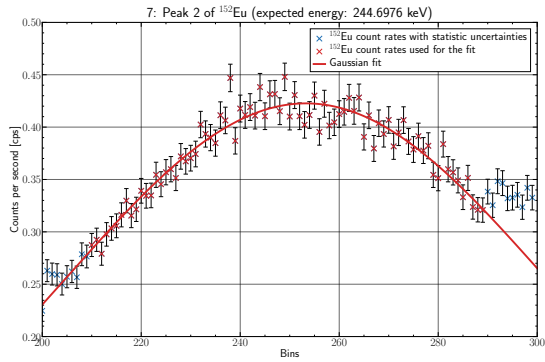
(a) Fit parameters, reduced χ -square test and expected energy for peak 3 of ^{60}Co .

¹⁵²Eu Peaks



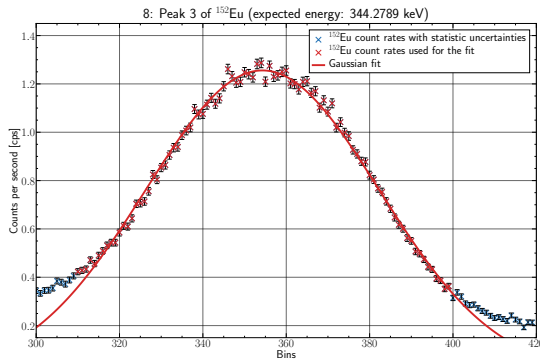
A [cps]	2.622	\pm	0.005
μ	118.93	\pm	0.05
σ	24.50	\pm	0.06
χ^2_ν	9.36		
E [keV]	121.7818		

(a) Fit parameters, reduced χ -square test and expected energy for peak 1 of ¹⁵²Eu.



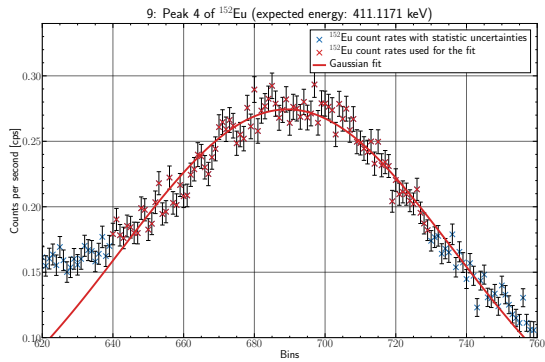
A [cps]	0.423	\pm	0.002
μ	253.3	\pm	0.4
σ	48.4	\pm	0.9
χ^2_ν	0.988		
E [keV]	244.6976		

(b) Fit parameters, reduced χ -square test and expected energy for peak 2 of ¹⁵²Eu.



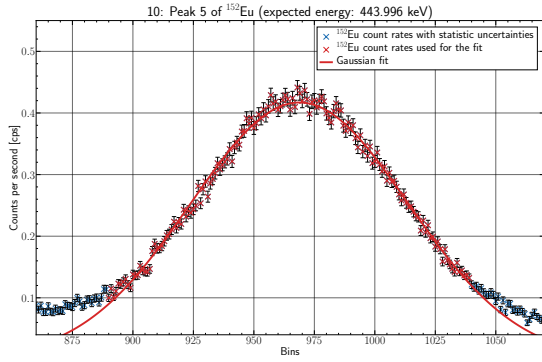
A [cps]	1.256	\pm	0.003
μ	354.29	\pm	0.07
σ	28.00	\pm	0.09
χ^2_ν	2.37		
E [keV]	344.2789		

(a) Fit parameters, reduced χ -square test and expected energy for peak 3 of ¹⁵²Eu.

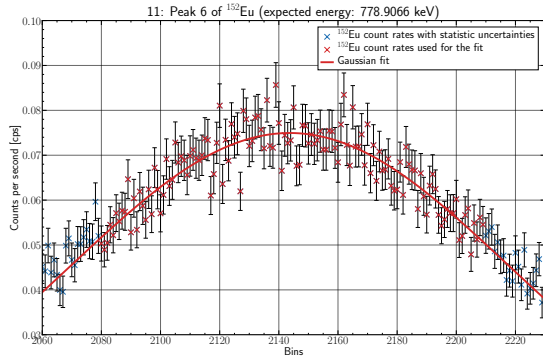


A [cps]	0.2744	\pm	0.0016
μ	689.3	\pm	0.4
σ	47.2	\pm	0.7
χ^2_ν	1.47		
E [keV]	411.1171		

(b) Fit parameters, reduced χ -square test and expected energy for peak 4 of ¹⁵²Eu.

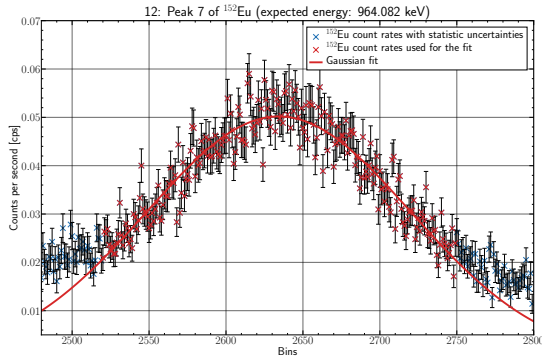


A [cps]	0.4170	\pm	0.0015
μ	968.82	\pm	0.15
σ	45.00	\pm	0.18
χ^2_ν	1.45		
E [keV]	443.996		

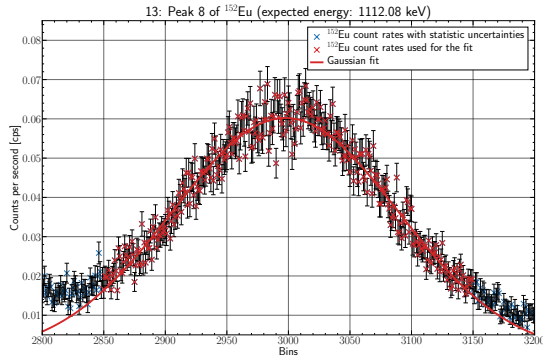


A [cps]	0.0750	\pm	0.0006
μ	2143.7	\pm	0.9
σ	73.9	\pm	2.0
χ^2_ν	0.893		
E [keV]	778.9066		

(a) Fit parameters, reduced χ -square test and expected energy for peak 5 of ^{152}Eu . (b) Fit parameters, reduced χ -square test and expected energy for peak 6 of ^{152}Eu .

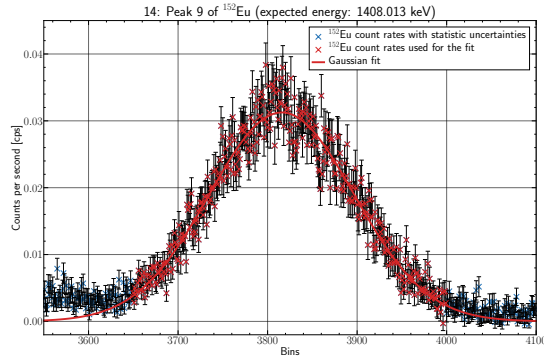


A [cps]	0.0502	\pm	0.0004
μ	2634.3	\pm	0.7
σ	85.8	\pm	1.1
χ^2_ν	1.19		
E [keV]	964.082		



A [cps]	0.0602	\pm	0.0004
μ	2997.5	\pm	0.6
σ	91.4	\pm	0.7
χ^2_ν	1.08		
E [keV]	1112.08		

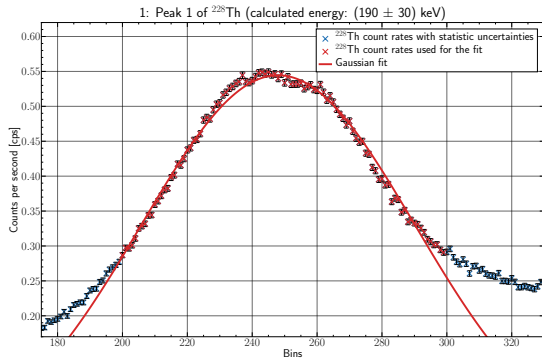
(a) Fit parameters, reduced χ -square test and expected energy for peak 7 of ^{152}Eu . (b) Fit parameters, reduced χ -square test and expected energy for peak 8 of ^{152}Eu .



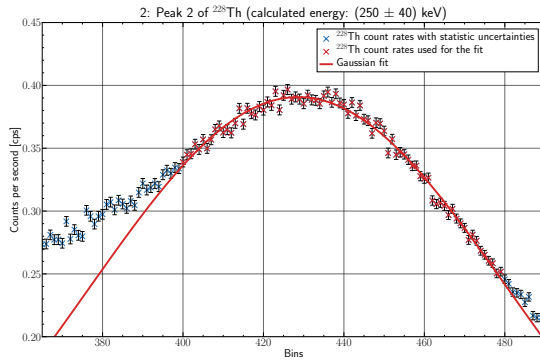
A [cps]	0.0313	\pm	0.0003
μ	3815.7	\pm	0.7
σ	81.0	\pm	0.6
χ^2_ν	1.05		
E [keV]	1408.013		

(a) Fit parameters, reduced χ -square test and expected energy for peak 9 of ^{152}Eu .

^{228}Th Peaks

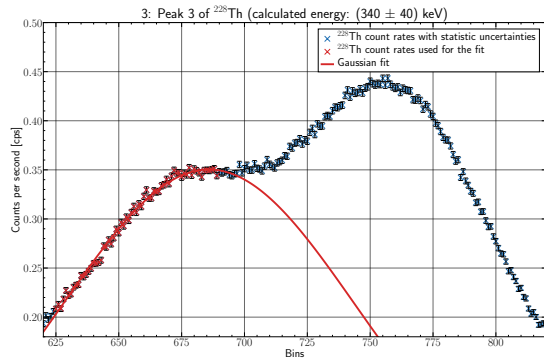


A [cps]	0.5445	\pm	0.0008
μ	247.98	\pm	0.07
σ	42.16	\pm	0.11
χ^2_ν	5.11		
E [keV]	190	\pm	30



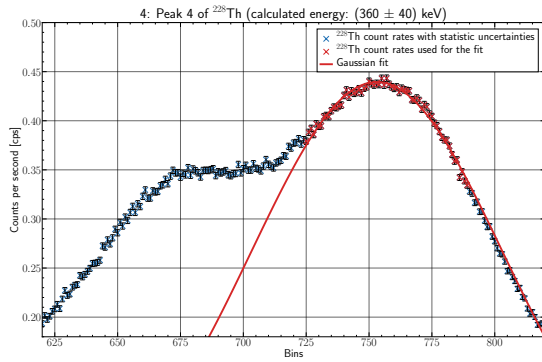
A [cps]	0.3907	\pm	0.0006
μ	428.7	\pm	0.2
σ	52.4	\pm	0.4
χ^2_ν	1.56		
E [keV]	250	\pm	40

(a) Fit parameters, reduced χ -square test and expected energy for peak 1 of ^{228}Th . (b) Fit parameters, reduced χ -square test and expected energy for peak 2 of ^{228}Th .



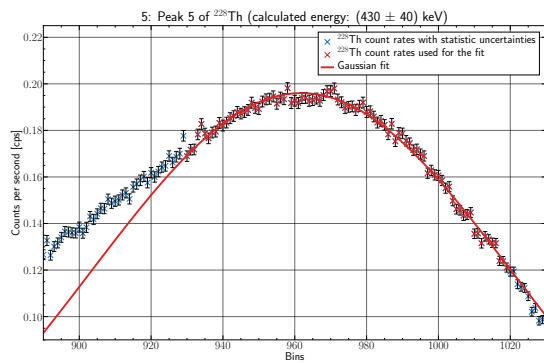
A [cps]	0.3503	\pm	0.0010
μ	685.8	\pm	0.8
σ	58.3	\pm	0.9
χ^2_ν	1.77		
E [keV]	340	\pm	40

(a) Fit parameters, reduced χ -square test and expected energy for peak 3 of ^{228}Th .



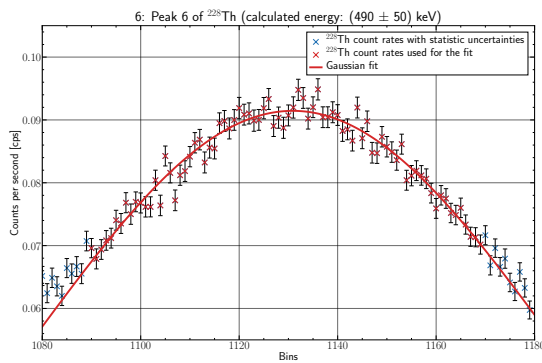
A [cps]	0.4394	\pm	0.0006
μ	753.12	\pm	0.15
σ	50.0	\pm	0.4
χ^2_ν	1.73		
E [keV]	360	\pm	40

(b) Fit parameters, reduced χ -square test and expected energy for peak 4 of ^{228}Th .



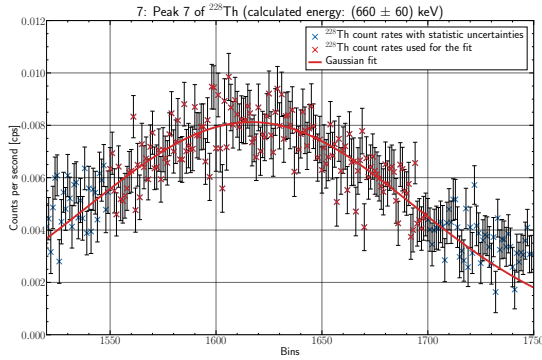
A [cps]	0.1960	\pm	0.0004
μ	961.9	\pm	0.3
σ	58.8	\pm	0.5
χ^2_ν	1.11		
E [keV]	430	\pm	40

(a) Fit parameters, reduced χ -square test and expected energy for peak 5 of ^{228}Th .

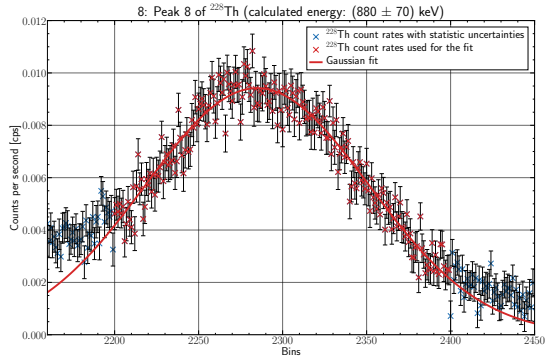


A [cps]	0.0914	\pm	0.0003
μ	1130.9	\pm	0.3
σ	52.4	\pm	0.7
χ^2_ν	1.14		
E [keV]	490	\pm	50

(b) Fit parameters, reduced χ -square test and expected energy for peak 6 of ^{228}Th .

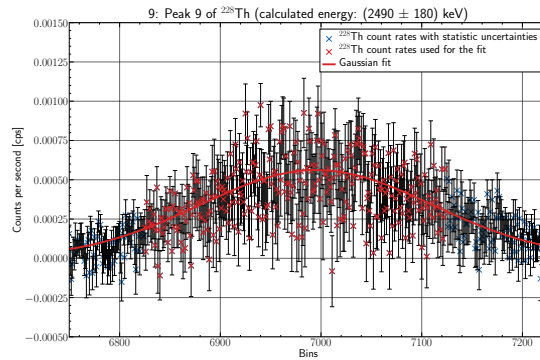


A [cps]	0.00812 ± 0.00011
μ	1616.7 ± 1.6
σ	77.0 ± 3.0
χ^2_{ν}	0.946
E [keV]	660 ± 60



A [cps]	$0.00942 \pm 8\text{e-}05$
μ	2284.9 ± 0.7
σ	66.6 ± 0.8
χ^2_{ν}	0.965
E [keV]	880 ± 70

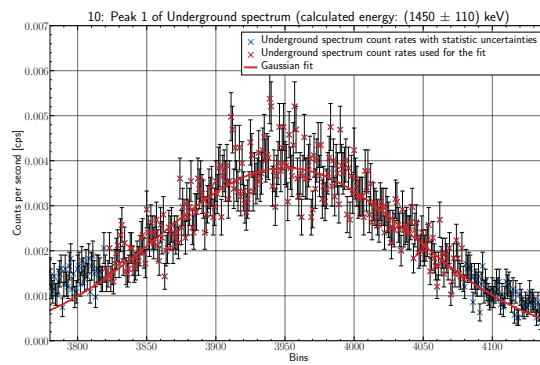
(a) Fit parameters, reduced χ -square test and (b) Fit parameters, reduced χ -square test and expected energy for peak 7 of ^{228}Th .
 (a) Fit parameters, reduced χ -square test and (b) Fit parameters, reduced χ -square test and expected energy for peak 8 of ^{228}Th .



A [cps]	$0.000562 \pm 1.8\text{e-}05$
μ	6995.0 ± 4.0
σ	115.0 ± 6.0
χ^2_{ν}	0.966
E [keV]	2490 ± 180

(a) Fit parameters, reduced χ -square test and expected energy for peak 9 of ^{228}Th .

Underground Peak



A [cps]	$0.00384 \pm 5e-05$
μ	3950.5 ± 1.1
σ	91.5 ± 1.5
χ^2_ν	1.16
E [keV]	1450 ± 110

(a) Fit parameters, reduced χ -square test and expected energy for the underground peak.

A.3 Lab Notes

Szintillator 15.08.22 - 16.08.22

NaI-Szintillator
 connect preamp of NaI to main amplifier

When connecting to oscilloscope: add resistance to input so no signal was back

connect main amp to oscilloscope: set sleeping time to 1 μ s
 observed from oscilloscope: ca. 1,3 μ s

connect to mult: channel analyzer (MCA)

adjust (energy) amplitude by setting coarse gain and gain

selected settings: coarse gain: 20
 gain: 2, scale from 0,5 to 1,5: $2 \pm 0,7$ gain

observed peaks: Peak 1: 2619 (channel number)
 Peak 2: 6937 "

for these settings, the highest thorium-peak is expected at channel number of ca. 14000 - 16000 (2740 keV)

measure 5 min Na-22 at maximum bin number
 calculate expected value for 30 min measurement
 to have a uncertainty of under 2% for the larger peak: select 8190 bins
 relative
 -> small peak: rel. uncertainty $\approx 5\%$

measure: Na 22: 30 bins 1790, 342 s
 Co 60: 40 bins 2450, 364 s
 E1 152: 60 bins 3660, 884 s
 background: 17877, 1029 s

} select times to have low rel. uncertainty for peaks

16.08.22

connect NaI amp to SCA, SCA to linear gate as trigger
 amp to linear gate as output -> MCA

use spectrum of NaI (MCA) to select energy range, so that only the first & Na-22 peak (511 keV) is visible

selected range: $E = 1,30$
 $\Delta E = 0,50$

connect plastic pre amp to amp, amp to oscilloscope
 estimated sleeping time: ca. 5 ns
 selected sleeping time: 0,5 μ s (lowest possible value)

connect plastic amp bipolar signal to SCA
 select whole energy range (check with MCA)

connect: negative output of NaI-SCA to timing unit
 " " plastic-SCA "

connect both timing unit outputs with coincidence unit (CU)

connect ~~min~~ neg. output of CU to oscilloscope

oscilloscope: - both signals occurred roughly at the same time (no systematic delay observable)
 => set delay to zero for both SCA
 - both signals widths were adjusted to 2 μ s (to avoid false signals, when there is only minimal overlap)

connect output of CU to hex counter
 add resistance to hex counter TTL (to avoid double signal)
 select ~~measuring time~~ measuring time: ~~100000ms~~ 100 000ms ($\approx 100s$)

adjust gain of plastic amp =

more gain $\hat{=}$ higher count rates \Rightarrow lower relative error

but also: more gain $\hat{=}$ more noise from plastic scintillator (\rightarrow false signals)

when adjusting: at oscillator: set trigger to NiJ ~~scintillator~~ scintillator, as those are the 511 keV-signals (SCA)
 observe ~~whether~~ whether noise from plastic is too high

~~SCA~~: try to maximize count rate without adding too much noise

selected: ~~fine~~ plastic amp ~~gain~~ coarse gain = 50
 " " gain: ~~6~~ (scale from 0,5 1,5) \Rightarrow ~~6~~ $\hat{=} 1,1$

measurement angle:
 measurement time: 100 000 ms each | Coarse gain: 50
 gain: 6 $\hat{=} 1,1$

angle	count rate
-50°	24
-45°	43
-40°	40
-35°	35
-30°	51
-25°	39
-20°	47
-15°	43
-10°	31
-9°	41
-8°	37
-7°	50
-6°	40
-5°	44
-4°	33
-3°	53
-2°	60
-1°	97
0°	155
1°	
2°	
3°	
4°	
5°	
6°	
7°	
8°	
9°	
10°	

angle	count
90°	9
85°	12
80°	8
75°	6
70°	6
65°	13
60°	3
55°	13
50°	10
45°	12
40°	8
35°	8
30°	9
25°	10
20°	15
15°	16
10°	33
9°	33
8°	107
7°	164
6°	136
5°	227
4°	249
3°	216
2°	225
1°	223
0°	181
-1°	126

-2°	88
-3°	56
-4°	36
-5°	12
-6°	17
-7°	16
-8°	10
-9°	7
-10°	7
-15°	15
-20°	8
-25°	13
-30°	19
-35°	6
-40°	8
-45°	12
-50°	9
-55°	9

estimated error:
 numbers that looked: 0,1°
 (multiples of 5°)
 others: 0,2°

Handwritten signature